LA-12567-MS

UC-420
Issued: December 1993

Scaling of Sustained ZT-40 M Reversed-Field Pinches

A. Haberstich
D. A. Baker
C. J. Buchenauer
E. J. Caramana
J. N. DiMarco
R. M. Erickson
J. C. Ingraham
A. R. Jacobson
E. M. Little
R. S. Massey
J. A. Phillips
K. F. Schoenberg
A. E. Schofield
K. S. Thomas
R. G. Watt
P. G. Weber

Los Alamos
NATIONAL LABORATORY
Los Alamos, New Mexico 87545

CONTENTS

ABSTRACT		1
I.	INTRODUCTION	1
II.	FACILITY	3
	A. Front End	3
	B. Diagnostics	4
III.	STANDARD MODE OF OPERATION	5
	A. Measurements	5
	B. Discharge Conditions	6
	C. Reproducibility	8
IV.	ELECTRON TEMPERATURE AND DENSITY	8
	A. Time Scans	8
	B. Current Scans	9
	C. Derived Parameters	10
V.	PLASMA RESISTIVITY	11
	A. Definitions	11
	B. Results	14
VI.	ENERGY CONTAINMENT TIME AND POLOIDAL BETA	14
	A. Plasma Energy	15
	B. Power Loss and Energy Containment Time	15
	C. Poloidal Beta	16
	D. Results	17
	E. Form Factor	17
VII.	IMPURITY LEVEL, PARTICLE LOSS RATE, AND RECYCLING	19
	A. Radiation from Low-Z Impurities	19
	B. Recycling of Deuterium	20
	C. Total Radiated Power	21
VIII.	OPERATION WITHOUT POLOIDAL LIMITERS	22

IX. OTHER SCALINGS 23
A. Pressure Scans 23
B. Early Discharge Time 24
C. Comparison With Standard Results 25
D. Constant I_ϕ/N_e 25

X. CONCLUSIONS 26

XI. ACKNOWLEDGMENTS 27

XII. REFERENCES 28

SCALING OF SUSTAINED ZT-40M REVERSED-FIELD PINCHES

by

A. Haberstich[†], D. A. Baker[†], C. J. Buchenauer, E. J. Caramana[†], J. N. DiMarco, R. M. Erickson, J. C. Ingraham, A. R. Jacobson[†], E. M. Little[†], R. S. Massey, J. A. Phillips, K. F. Schoenberg[†], A. E. Schofield, K. S. Thomas[†], R. G. Watt, and P. G. Weber[†]

ABSTRACT

Experiments aimed at evaluating the scaling properties of the ZT-40M Reversed-Field Pinch (RFP) facility were conducted in 1983 at Los Alamos. Sustained discharges were produced at nominal toroidal currents ranging from 60 to 240 kA. The standard fill pressure was kept close to the lower limit of the usable pressure range, and the scaling data were acquired at a fixed time in the discharges while the plasma was in a quasi-steady state. Scalings of the diameter-averaged electron density, electron temperature on axis, product of these two parameters, and of various definitions of the electrical resistivity are presented. Trends of the toroidal voltage, energy containment time, and poloidal beta are shown. The impurity contents, particle containment time, and total radiation losses are described, and results obtained with and without poloidal limiters are compared. In addition, the performance of the facility at higher than standard density and at a constant ratio of the toroidal current over the electron line density is examined.

I. INTRODUCTION

This report gives an account of a series of scaling measurements performed in 1983 on the ZT-40M Reversed-Field Pinch (RFP) facility at Los Alamos. These experiments were carried out to gather information necessary to evaluate the potential of the ZT-40M concept for a future

---

[†] ZT-40M Scaling Team

fusion reactor. These data were also of interest for comparison of the performance of ZT-40M with that of other RFP facilities.

The effort was focused on the measurement of significant plasma parameters and on the determination of their scaling with the discharge current. The strategy was to gather the data under a standard set of discharge conditions, at a fixed time in the discharges. The measurements were made at as close to a steady state as possible, and, to help ensure reliable results, each reading was averaged over several identical discharges.

The 1983 scaling experiments were carried out over a cumulative period of three and a half months, apportioned as follows:

Phase I(a)	Jan. 5 – Jan. 28
Phase I(b)	Feb. 17 – Mar. 3
Phase II	May 6 – June 10
Phase III	June 24 – July 15
Phase IV	Dec. 13 – Dec. 21

Since some of the experimental conditions varied in the course of this sequence, the phases during which the measurements were made are identified for each of the results presented in the report.

The document includes a brief description of the facility and a discussion on the selection of a standard mode of operation. Results obtained with and without poloidal limiters are presented. These include measurements of the electron density and temperature; determinations of the products of these two parameters; calculations of the electrical resistivity, poloidal beta, and energy containment time; and spectroscopic observations. Data obtained at higher than standard electron densities and at a constant ratio of the toroidal current over the electron line density are also discussed. The main results are summarized at the end of the report.

The interpretation of the data is based on the experimental and theoretical knowledge available at the time of the study. In fact, much of the present work was shown at the RFP Workshop held at Los Alamos, June 13–16, 1983, and at the November 1983 meeting of the American Physical Society.[1,2]

Extensive experimental and theoretical RFP research has been conducted at Los Alamos and at other laboratories since the conclusion of this scaling study. A great deal has been learned, for example, about the internal and edge properties of the plasma. Information about how these properties scale with the discharge current may help explain the observations made in this report.

II. FACILITY

The ZT-40M facility included the front end, where the plasma experiments took place; the vacuum, power supply, and control systems; and the diagnostics and data acquisition systems. Features of the front end and diagnostics systems of significance to the interpretation of the present work are discussed below.

A. Front End

The toroidal discharge chamber had a major radius of 114 cm and a minor radius of 20 cm. This chamber, also referred to as the liner, consisted of 12 Inconel bellows sections interspersed with 12 recessed Inconel diagnostics sections. Mounted on the diagnostics sections were access ports in various sizes and configurations. The chamber was centered in a 2-cm-thick toroidal aluminum shell with an inner minor radius of 22 cm. The purpose of the shell was to promote stability as well as short-term equilibrium of the discharges. The shell had a toroidal and a poloidal gap to allow the penetration of magnetic fields produced by external poloidal and toroidal windings. Twelve laminated silicon-iron cores coupled the toroidal winding current to the toroidal plasma current. Trim coils allowed the application of axisymmetric vertical and horizontal magnetic fields to control long-term equilibrium.

The toroidal current was generated by two capacitor banks. A fast bank created the toroidal current with a rise time of a fraction of a millisecond, and a power-crowbar bank controlled the slope of the plasma current during the sustainment period of the discharge. The toroidal field was produced by three similar banks. A first bank generated the toroidal bias magnetic field in the discharge chamber before the toroidal current was applied. The second bank produced the reversal of the toroidal field at the edge of the discharge, on a time scale comparable to the rise time of the toroidal current, and a power-crowbar bank controlled the reversed field during the sustainment period.

The facility was operated with deuterium, which was introduced in the discharge chamber approximately 40 s before initiation of the discharges. During some of the Phase I experiments, gas injection was used to supplement the initial gas fill. The intent was to maintain a constant electron density during the sustainment period. Because of poor reproducibility at high currents, the results of these attempts are not discussed in this report.

ZT-40M underwent several modifications before and during the scaling study. These improvements were in the areas of field error corrections,[3] equilibrium control,[4] and wall protection.[5] Whereas Phase I(a) experiments were conducted without equilibrium feedback, Phase I(b) and subsequent experiments benefitted from active feedback in the positioning of the magnetic flux surface at the poloidal gap.[4] Feedback control made a significant improvement in the reproducibility of the discharges and helped speed up the acquisition of usable data.

The discharge chamber was protected by four poloidal graphite limiters during Phases I and II.[5] These limiters were located at stations 1, 4, 7, and 10 in Fig. 1 and protruded approximately 0.95 cm into the edge region of the plasma. The poloidal limiters were removed following Phase II, and the experiments were conducted without limiters during Phases III and IV.

Gradual changes in the performance of the facility during the study have been linked to the conditioning of the discharge chamber following vacuum openings. Phase I was preceded by several openings for the testing of various wall protection schemes. The discharge chamber was also opened between Phases I and II for the installation of a Thomson-scattering viewing dump and, as already mentioned, between Phases II and III for the removal of the poloidal limiters. Phase IV followed a major repair of the discharge chamber.

B. Diagnostics

The electrical diagnostics were located in the interspace between the liner and the equilibrium shell. The sensors running in the poloidal direction were installed in the valleys of the bellows liner (as seen from the outside), and those following the major circumference of the torus ran over the peaks of the liner. The locations of these diagnostics can be visualized with the help of Fig. 1.

- Two Rogowski coils measured the sum of the toroidal plasma and liner currents. The sensor used in the study was located between stations 8 and 9.

- Several flux loops measured the enclosed toroidal magnetic flux. One of the two loops used in the study was located between stations 10 and 11, and the other between stations 4 and 5.

- Voltage loops traced the major circumference of the experiment at four poloidal locations. They gave a reading of the toroidal voltage and were also used to monitor the global equilibrium position of the discharge.

- Two extended pickup coils measured the toroidal magnetic field over a toroidal distance of 82 cm. The coil used in the study was mounted at the outer midplane of the torus at station 9.

The figure also shows the locations of the plasma diagnostics used in the study. These included the following systems.

- A multichord infrared (IR) interferometer, running at 10.6 μm, measured the line-integrated electron density along eight vertical chords.[6] Because of mechanical vibrations setting in at 2 to 3 ms into the discharges, the validity of these measurements was confined to early discharge times.

- A vibration-compensated, single-chord, two-color interferometer operating at 10.6 and 0.6328 μm measured the line-integrated electron density along a vertical minor diameter of the discharge chamber.[7]

- A single-chord far-infrared (FIR) interferometer running at 184.6 μm measured the line-integrated electron density along a vertical chord of the discharge.[8]

- A single-point, single-time Thomson-scattering diagnostic operating at the ruby wavelength of 694.3 nm measured the electron temperature and relative density on the minor axis of the discharge and, in a few cases, at 14.3 cm below the minor axis of the discharge.

- An array of quartz-ultraviolet/visible (QUV/V) spectrometers viewed impurity radiation along six vertical chords, at wavelengths ranging approximately from 200 to 600 nm.

- An absolutely calibrated vacuum-ultraviolet (VUV) spectrometer, located at the outer midplane of the experiment, measured the radiation emitted by low-Z impurities at wavelengths ranging from 40 to 125 nm. The instrument was on loan from Johns Hopkins University.[9]

- A set of four absolutely calibrated Balmer-alpha (D_α) monitors operating at 656.1 nm observed deuterium-recycling processes at variable locations around the major circumference of the experiment.

- A bolometer probe, mounted on top of the torus, provided a local absolute measurement of the plasma radiation losses.[10]

III. STANDARD MODE OF OPERATION

The scaling results presented in Sections IV through VIII were acquired in the so-called standard mode of operation. Some of the results shown in Section IX were obtained under nonstandard conditions. The following description of the standard mode of operation addresses two issues: the conditions under which the measurements were made and the conditions under which the discharges were produced. The reproducibility of the discharges obtained in the standard mode of operation is considered at the end of this section.

A. Measurements

Most of the scaling data were collected while the discharges were in a quasi-steady state. This state is defined as a condition in which the discharge current and the applied toroidal field are kept essentially constant in time, while the electron density and temperature are allowed to vary on a time scale longer than the particle and energy containment times. The density can

decay more slowly than predicted by the particle containment time, because of recycling from the wall of the discharge chamber.

The scaling measurements and analyses were performed at a fixed time in the discharges. A consequence of this approach is that the results are dependent on the time chosen for the measurements and on the chosen set of discharge conditions. Among the affected parameters are the electron density, electron temperature, and electrical resistivity, which enter into the calculations of the poloidal beta and energy confinement time.

An alternative would have been to perform the measurements and analyses with a constraint on one of the plasma parameters, such as the electron density. Presumably, this method would have been less sensitive to the mode of operation. A tentative result obtained in this manner is discussed briefly in Section IX.

With the exception of the Thomson scattering measurements, the data were acquired over the entire duration of the discharges. The data used in the analyses have been smoothed in time to reduce the effect of high-frequency fluctuations. The results reported here represent averages over several shots, and the accompanying error bars depict standard deviations from these averages. Scaling laws, when shown, are weighted least-squares fits to the logarithms of the data.

Electron temperature measurements took place at a single time in the discharges. Averaging the Thomson-scattering data over several discharges consisted of averaging the readings of each of the six spectral channels of the diagnostic and of fitting the results to a theoretical spectral distribution. This distribution is a Maxwellian modified by a relativistic correction factor. The fit allows two degrees of freedom: (1) the area under the curve that gives a measure of the electron density and (2) the width of the distribution that determines the electron temperature. The error bars correspond to the chi-squared errors generated during the curve fitting and, therefore, give an indication of how well the averaged data fits the theoretical distribution.

The discharge times are specified from the onset of the toroidal bias field. The discharge currents are defined either as the nominal discharge currents (60, 90, 120, 180 or 240 kA) or as the discharge currents at the time of a measurement. What is labelled the discharge current in the figures in this document is, in fact, the sum of the toroidal plasma and liner currents. The approximation is justified since the liner current was much smaller than the plasma current at the times of interest.

B. Discharge Conditions

The chosen method of RFP formation was the so-called matched mode illustrated in Fig. 2 (solid curves). In this mode, a toroidal bias field is first created in the discharge chamber. The toroidal voltage, applied at the peak of the bias field, then ionizes the gas and produces the toroidal discharge current. The discharge's tendency to self-reverse is assisted by the reversal of

the applied toroidal field. This reversal takes place on the same time scale as the rise of the toroidal current. The magnitude of the bias field is adjusted so that the toroidal flux remains constant during the reversal. This keeps the poloidal current in the liner small and the toroidal fields in and outside the liner matched.

The formation of the discharge is followed by a sustainment period during which the toroidal current is flat topped and the toroidal-field reversal at the wall is maintained by the power supply power-crowbar circuits. The toroidal magnetic flux, which would otherwise diffuse out of the plasma volume, is sustained by an internal plasma mechanism referred to as the dynamo effect. This phenomenon is described in Section V. As seen in Fig. 2, the sustainment period began approximately 2 ms after onset of the toroidal bias field.

The pinch parameters F and Θ are defined, respectively, as the ratios of the toroidal and poloidal magnetic fields at the edge of the discharge over the cross-sectional average of the toroidal magnetic field. The value of F is controlled by the magnitude of the toroidal field reversal at the edge of the discharge, and the value of Θ is observed experimentally to be controlled by F. This coupling can be described in terms of the so-called Modified Bessel Function Model (MBFM) discussed in Section V. During a previous rise-time study, a value of approximately 1.5 had been used for Θ.[11] Since it was known that operation at high Θ could lead to a regime of sawtooth oscillations, a value of less than 1.5 was chosen for the scaling study.

Running the experiment at an excessively high or low fill pressure produced the results illustrated by the dashed and dot-dashed curves in Fig. 2. High-pressure operation resulted in an early dip in the toroidal current, caused by the large electrical resistance of the discharge. This dip was accompanied by a drop in the reversed toroidal field that eventually led to a loss of reversal and to an early termination. An excessively low fill pressure produced a condition wherein the pinch no longer reversed. The interval separating these extreme fill pressures is referred to as the usable fill-pressure range. The standard discharge condition, illustrated by the solid curve in the figure, was obtained by operating the experiment near the lower limit of the usable fill-pressure range.

The rise-time study had shown that the usable fill-pressure range narrowed as the rise time of the toroidal current was increased.[11] A rise time of 0.75 ms was adopted for the scaling study. This value was deemed long enough to avoid excessive vibrations of the discharge chamber at high current, while remaining short enough to allow relatively large excursions from the standard fill pressure.

The nominal toroidal discharge currents were set at 120, 180, and 240 kA during Phase I and at 60, 90, 120, and 180 kA during Phases II through IV. The 180-kA limitation after completion of Phase I was to prevent excessive wear on the liner from plasma-wall interaction. The discharge current rise time was maintained at 0.75 ms for all levels of current.

The pinch parameters F and Θ were kept approximately constant as functions of discharge current. Values of F and Θ recorded during Phases I and II are shown in Figs. 3 and 4. The values of F ranged between -0.12 and -0.18; Θ ranged between 1.47 and 1.39.

The fill pressure was kept close to the lower limit of the usable range for the reasons elaborated on above. The pressures used during Phases I and II are plotted in Fig. 5. Their increase with current is seen to be somewhat weaker than linear. This fact is reflected in the rising ratio I_ϕ/N_o of the toroidal current over the neutral gas density per unit length of the torus (Fig. 6).

C. Reproducibility

The reproducibility of the data taken during a standard 180-kA run is illustrated by the superposition of twenty discharges in Fig. 7. The Phase I data include (a) the sum of the toroidal currents in the plasma and liner, (b) the applied toroidal magnetic field outside the liner, (c) the plasma's average toroidal magnetic field obtained from the measured toroidal magnetic flux, (d) the diameter-averaged electron density, measured with the two-color interferometer, (e) the ratio of the toroidal current I_ϕ over the electron line density N_e, assuming a uniform density distribution, and (f) the effective electrical resistivity on axis calculated with the help of the MBFM. Two of the discharges were intentionally terminated at 10 ms; the others were ended at 10.5 ms.

Reproducibility was not quite as good, but was still adequate, at the high and low ends of the discharge current range. As already mentioned, changes in the performance of the facility were observed as the study progressed. Phases I and II, and Phase III, were marked by gradual increases in the electron temperature and decreases in the electron density. These changes coincided with gradual cleanups of the discharge chamber.

IV. ELECTRON TEMPERATURE AND DENSITY

The data presented in Sections IV through VII were obtained during Phases I and II, while ZT-40M was operated with the four poloidal graphite limiters. Data obtained during Phase III, after the limiters had been removed, are discussed in Section VIII.

A. Time Scans

The evolution of the electron density as a function of time is shown in Fig. 8. These diameter-averaged densities, $\langle n_e \rangle_{dia}$, were obtained with the two-color interferometer over a period of 2 days during Phase II. The traces generated at nominal toroidal currents of 60, 90, 120, and 180 kA represent averages over all valid discharges produced during these runs.

Following an initial peak at 1 to 1.5 ms, the density is seen to decrease at a rate that itself decreases in time. The density eventually approaches a quasi-equilibrium wherein losses are approximately balanced by particles recycled from the liner wall. Recycling is discussed in more detail in Section VII.

Single-point Thomson-scattering measurements of the electron temperature on axis, T_{eo}, are shown in Fig. 9. Time scans and data averaging required a large number of identical discharges at each current level. These data were obtained over an effective running period of 6 days. The figure shows the electron temperatures obtained at several times in the discharges at nominal toroidal currents of 60, 120, and 180 kA. The initial temperature rise is governed not only by the time it took to heat the plasma, but also by the rapidly changing electron density early in the discharges.

The electron density and temperature are seen to settle down after a few milliseconds in the discharges. The time of 5 ms was chosen for most of the scaling measurements carried out in the standard mode of operation. The rates of change of the plasma parameters then satisfied the quasi-steady-state conditions.

B. Current Scans

Variations of the electron density and temperature with the discharge current, at 5 ms, are shown in Figs. 10 and 11. The open symbols represent data obtained in the course of various time scans performed during Phase I, and the solid symbols represent data taken during time, as well as current, scans during Phase II. The Phase I temperatures are produced by interpolation of 4- and 6-ms data.

The diameter-averaged electron densities measured during Phase II are lower than those obtained during Phase I, and the electron temperatures are higher. These effects are part of the gradual changes in performance mentioned earlier; they are believed to have been caused mainly by wall conditioning. Evidence of a similar cleanup effect during Phase III is presented in Section VIII. The small difference in fill pressure between Phases I and II is not sufficient to explain the different behaviors. The bearing that the fill pressure had on the plasma parameters is discussed in Section IX.

The Phase II results, which presumably were obtained in a better environment, are used to determine the density scaling. The Phase II electron densities, least-squares fitted over toroidal currents ranging from 60 to 120 kA, are found to scale as $I_\phi^{1.31}$, with a standard deviation of the exponent of $\pm$ 0.17. The density at 180 kA falls below this projection.

The discharge conditions and symbols used in the central electron temperature plot of Fig. 11 are the same as those in the density plot with the exception of a missing data point at the 240-kA level. The Phase II data, least-squares fitted over the 60- to 120-kA range, scale as $I_\phi^{0.55}$.

The standard deviation in this case is ± 0.06. This scaling also gives a reasonably good prediction of the temperature at 180 kA.

The electron temperatures observed during Phase I remain below 250 eV at all currents. The lack of temperature increase between 180 and 240 kA may have been influenced by the fact that the two measurements were performed during different runs. Unfortunately, the 240-kA measurement at this time in the discharge was not repeated.

Figure 12 shows the behavior of $<n_e>_{dia}T_{eo}$, the product of diameter-averaged electron density and central electron temperature, during Phases I and II. The discharge conditions and symbols are the same as in Fig. 11. An important feature of this result, already noted at the time of the measurements, is the tendency of the experiment to maintain constant products $<n_e>_{dia}T_{eo}$ at each current level in spite of differences in temperature and density. This feature reappears in other results in this report.

A least-squares fit of the combined Phase I and Phase II data over the 60- to 120-kA range gives a scaling proportional to $I_\phi^{1.95}$ with a standard deviation of ± 0.09. As one would expect from the density and temperature results, the data at 180 and 240 kA fall below this low-current scaling law.

C. Derived Parameters

A useful parameter for comparison of the regime of operation of ZT-40M with that of other RFPs is the ratio I_ϕ/N_e, where N_e is the electron line density per unit length of the torus.

To express the line density in terms of the measured diameter-averaged density, an electron density distribution of the form

$$n_e = n_{eo}\left[1-\left(\frac{r}{a}\right)^{\alpha}\right] \tag{1}$$

is assumed. Here, n_{eo} is the density on axis, r is the minor radial position, a is the minor radius of the liner, and α is a constant. The line density then becomes

$$N_e = \pi a^2 <n_e>_{dia} \frac{\alpha+1}{\alpha+2} \quad . \tag{2}$$

The values of I_ϕ/N_e, plotted in Fig. 13 as functions of the toroidal current, correspond to a parabolic density distribution. The conditions and symbols are the same as in Fig. 10. Except for a high reading at 60 kA, I_ϕ/N_e ranges between 0.7 and $1.3\cdot10^{-13}$ A-m. Because of the initial density pumpout, these values are significantly larger than the I_ϕ/N_o ratios that are based on the fill density.

A parameter of potential interest for predicting the stability of the discharges is the streaming parameter ξ, defined locally as $(J/en_e)/(kT_e/m_e)^{1/2}$, where J is the current density. With the electron density distribution of Eq. (2), the streaming parameter on axis becomes

$$\xi_o = \frac{J_{\phi o}}{J_\phi}\,\frac{I_\phi}{N_e}\,\frac{\alpha}{\alpha+2}\,\frac{1}{e}\,\left(\frac{m_e}{kT_{eo}}\right)^{1/2} \quad , \tag{3}$$

where $J_{\phi o}$ is the toroidal current density on axis and $J_\phi = I_\phi/\pi a^2$. The MBFM can be used to estimate the current density peaking factor $J_{\phi o}/J_\phi$. For a parabolic density distribution, one then obtains the streaming parameter plotted in Fig. 14. The discharge conditions and symbols are the same as in Fig. 11.

The radial dependence of ξ can be estimated from the above model with an assumption on the temperature distribution. For a typical 120-kA discharge with a temperature assumed to decrease with the fourth power of the minor radius, ξ gradually increases past a radius of 5 cm to double its value on axis at the MBFM transition radius of 16 cm. The variation of the streaming parameter beyond that point becomes sensitive to the details of the temperature and density distributions in the edge region.

V. PLASMA RESISTIVITY

The computation of plasma resistivity in the RFP is, in general, a complex and model-dependent process. The model dependence arises mainly from the lack of experimental information about the internal field structure of the pinch. In addition, the existence of a plasma dynamo, which is hypothesized to generate and maintain the toroidal magnetic field against resistive diffusion, can substantially affect the resistivity calculation.[12] As a result, several definitions of resistivity are usually invoked to gauge RFP performance. A comprehensive description and interpretation of RFP resistivity is given in Ref. 12.

A. Definitions

One straightforward way of estimating RFP plasma resistivity is to define the effective resistivity on the minor axis of the discharge as

$$\eta_{eff} = \frac{\langle E_z(0,t)\rangle}{\langle J_z(0,t)\rangle} \quad , \tag{4}$$

where

$$\langle E_z(0,t)\rangle = \langle E_z(a,t)\rangle - \frac{\partial}{\partial t}\int_0^a \langle B_\theta(r,t)\rangle\, dr \quad . \tag{5}$$

Cylindrical coordinates are used explicitly in this section; the coordinate z has been substituted for the coordinate ϕ used in the other sections of the report. $E_z(0,t)$ and $J_z(0,t)$ represent the electric field and the current density on axis, respectively; $B_\theta(r,t)$ denotes the poloidal magnetic field; r is the minor radial coordinate; and $< >$ denotes a smoothing in time.† It is assumed that $\langle \boldsymbol{B} \rangle$, $\langle \boldsymbol{J} \rangle$ and $\langle \boldsymbol{E} \rangle$ are azimuthally symmetric and that they self-consistently satisfy Faraday's law

$$\nabla \times \langle \boldsymbol{E} \rangle = - \frac{\partial}{\partial t} \langle \boldsymbol{B} \rangle \tag{6}$$

and the force-free MBFM[12]

$$\mu_o \langle \boldsymbol{J} \rangle = \nabla \times \langle \boldsymbol{B} \rangle = \lambda(r) \langle \boldsymbol{B} \rangle \quad . \tag{7}$$

The factor $\lambda(r)$ is a constant λ_o up to a transition radius r_t and decreases linearly to 0 between r_t and the radius of the discharge chamber.

The effective resistivity, η_{eff}, uses $\boldsymbol{E} = \eta \boldsymbol{J}$ as the simplified plasma Ohm's law. However, by neglecting other Ohm's law components, such as the Lorentz electric field $\boldsymbol{u} \times \boldsymbol{B}$ driven by fluctuations, η_{eff} can have anomalously large values. For example, present generation RFP discharges are sustained by voltage sources that produce a positive toroidal electric field at the wall, $E_z > 0$, while keeping the poloidal field at the wall near zero, $E_\theta \cong 0$. This sustainment is inconsistent with global and one-dimensional transport codes that predict the loss of field reversal on time scales that are much shorter than observed discharge lifetimes.[13] One way of reconciling this discrepancy is to hypothesize that plasma fluctuations significantly contribute to Ohm's law through the term $\boldsymbol{u} \times \boldsymbol{B}$ where $\boldsymbol{u}$ is the time-dependent fluid velocity. In this model, during the steady-state or "sustainment" phase of the discharge, the mean poloidal current is driven by fluctuations. The process of sustaining poloidal plasma current by means of a toroidal electric field and current is termed the dynamo effect.[14,15]

A more accurate estimate of resistivity, one which explicitly accounts for fluctuations, can be drawn from the global quantities of magnetic energy and helicity. With the magnetic energy inside the discharge chamber defined as $W = (2\mu_o)^{-1} \int \boldsymbol{B}^2 \, dV$, the energy balance inside the RFP is described by Poynting's theorem:

---

† For the discharges examined in this section, the smoothing takes the form

$$\langle \boldsymbol{B}(t) \rangle = \tau^{-1} \int_{t-\tau/2}^{t+\tau/2} \boldsymbol{B}(t') \, dt' \quad ,$$

where $\tau \cong 0.25$ ms.

$$\frac{\partial W}{\partial t} = -\frac{1}{\mu_o}\int \boldsymbol{E}\times\boldsymbol{B}\cdot d\boldsymbol{S} - \int \boldsymbol{E}\cdot\boldsymbol{J}\,dV \quad . \tag{8}$$

In terms of the mean power flow, Eq. (8) reduces to[12]

$$\begin{aligned}\frac{\partial <W>}{\partial t} &= \frac{\partial}{\partial t}\left(\frac{1}{2\mu_o}\int <\boldsymbol{B}>^2 dV\right)\\ &= I_z V_z - I_\theta V_\theta - \int [\eta_\parallel(<J_\parallel>^2 + <\delta J_\parallel^2>) + \eta_\perp <\delta J_\perp^2> - <\boldsymbol{u}\times\boldsymbol{B}\cdot\boldsymbol{J}>]\,dV\\ &\equiv I_z V_z - I_\theta V_\theta - \int \eta_\parallel^{w} <J_\parallel>^2 dV \quad ,\end{aligned} \tag{9}$$

where I_θ denotes the poloidal current in the toroidal field coil; I_z, V_z, and V_θ are, respectively, the total toroidal plasma current and the toroidal and poloidal loop voltages measured across shell gaps at $r = a$; $\eta_\parallel$ and $\eta_\perp$ denote the resistivities parallel and perpendicular to the magnetic field,[16] and δ is the fluctuation operator.

Similarly, magnetic helicity is defined as the "knottedness" of the magnetic field lines within the toroidal discharge chamber,[15] excluding the coupling of plasma fields with externally linked transformer fields.[17] That is, $K = \int (\boldsymbol{A} - \boldsymbol{A}_t)\cdot\boldsymbol{B}\,dV$, where $\boldsymbol{A}$ is a total magnetic vector potential resulting from all currents in the RFP system, whereas $\boldsymbol{A}_t$ results from currents in the poloidal field transformer coils and associated image currents in the conducting shell surrounding the plasma. By defining $\boldsymbol{A}_t$ in this manner, one has $\int \boldsymbol{A}_t\cdot\boldsymbol{B}\,dV = \Phi\Psi$ where Φ denotes the RFP toroidal flux and Ψ denotes the external poloidal flux threading the central hole of the torus.

The mean helicity flow in the RFP is given by[12]

$$\begin{aligned}\frac{\partial <K>}{\partial t} &= \frac{\partial}{\partial t}\int <\boldsymbol{A} - \boldsymbol{A}_t>\cdot<\boldsymbol{B}>\,dV\\ &\cong 2\phi V_z - 2\int \eta_\parallel(<\boldsymbol{J}>\cdot<\boldsymbol{B}> + <\delta\boldsymbol{J}\cdot\delta\boldsymbol{B}>)\,dV\\ &\equiv 2\phi V_z - 2\int \eta_\parallel^{k} <\boldsymbol{J}>\cdot<\boldsymbol{B}>\,dV \quad .\end{aligned} \tag{10}$$

In Eqs. (9) and (10), $\eta_\parallel^{w}$ and $\eta_\parallel^{k}$ denote effective resistivities based on global power and helicity balances. As stated in Ref. 12, there is reason to believe that the term $-\int <\boldsymbol{u}\times\boldsymbol{B}\cdot\boldsymbol{J}>\,dV$ is a positive definite quantity and that the positive definite terms $<\delta J_\parallel^2>$ and $<\delta J_\perp^2>$ are larger in comparison with $<J^2>$, than is $<\delta\boldsymbol{J}\cdot\delta\boldsymbol{B}>$ in comparison with $<\boldsymbol{J}>\cdot<\boldsymbol{B}>$. Hence, $\eta_\parallel^{k}$ is hypothesized to be a better estimate of parallel Spitzer resistivity than is $\eta_\parallel^{w}$.

B. Results

Figures 15 through 17 illustrate the resistivity analysis of Phase I and Phase II scaling runs. Measured toroidal voltages, which enter these calculations, are shown in Fig. 18. The resistivities η_o^w and η_o^k are obtained by solving Eqs. (9) and (10) for $\eta_\parallel^w$ and $\eta_\parallel^k$, assuming the spatial dependence $\eta_\parallel^{w,k} = \eta_o^{w,k}[1-(r/a)^\nu]^{-3/2}$. In Fig. 15, the values of η_o^w and η_o^k assume $\nu=2$, whereas in Fig. 16 the lower and upper bounds on η_o^k represent parabolic ($\nu=2$) and quartic ($\nu=4$) temperature profiles, respectively. These profiles provide the upper and lower bounds of tentative Thomson-scattering measurements of $T_e(r)$. The quantity η^o denotes the expected Spitzer parallel resistivity on axis based on Thomson-scattering data for an effective ionic charge Z_{eff} of 1. The parameter R_T, plotted in Fig. 17, denotes a global plasma resistance defined as

$$R_T = \frac{1}{I_z^2}\int \eta_\parallel^w <J>^2 dV \quad . \tag{11}$$

R_T is approximately equal to V_z/I_z during quasi-steady-state conditions at 5 ms.

In interpreting Figs. 15 and 16, there are several significant features to elucidate. The fact that η_o^w and η_o^k scale as $I_z^{-0.85}$ and T_{eo} scales as $I_z^{0.55}$ implies that η_o^w and η_o^k scale classically with temperature ($\propto T_{eo}^{-3/2}$). Furthermore, η_o^k is between 2 and 3.5 times η^o, assuming $Z_{eff}=1$. Most of this difference can probably be accounted for by oxygen impurities in the discharge;[18] hence, η_o^k is a reasonable estimator (within a factor of 2) of classical Spitzer resistivity. Finally, the effective resistivity on axis, η_{eff}, and the concomitant toroidal loop voltage V_z are significantly greater than the values obtained from the classical Ohm's law, $V_z = 2\pi R \eta^o J_z(0)$, where R is the major radius of the torus. This difference reflects the large local power absorption on axis where $<J>\cdot<E>$ is maximized to drive both the dynamo and local ohmic heating.

The toroidal current is labelled I_ϕ in Figs. 15 and 17 for consistency with the other illustrations in the report.

VI. ENERGY CONTAINMENT TIME AND POLOIDAL BETA

The global energy containment time τ_E is defined in terms of the plasma energy W_p and the total power loss from the plasma, P_L, as

$$\tau_E = \frac{W_p}{P_L} \quad . \tag{12}$$

Neither of the quantities appearing in Eq. (12) was measured directly in ZT-40M, so the energy containment time must be estimated indirectly.

A. Plasma Energy

The total plasma energy is the sum of the thermal energy $(3/2)k(n_eT_e + n_iT_i)$ and the energy in fluid motion that can be due to macroscopic drift motion and plasma turbulence. Fluid motion was not experimentally determined. It is assumed to have a negligible effect on the determination of τ_E.

The plasma thermal energy is therefore

$$W_p = \frac{3}{2}\int k(n_eT_e + n_iT_i)\,dV \quad , \tag{13}$$

where n_i and T_i are the ion density and temperature, and where the integral is taken over the plasma volume V.

Because of the lack of measurements of the spatial distributions of n_e, T_e, and T_i, the associated uncertainties are lumped into a form factor f which relates the integral of Eq. (13) to the measured quantities that are the electron temperature on axis and the diameter-averaged electron density. Thus, the form factor is given by

$$f \equiv \frac{<n_eT_e + n_iT_i>_V}{2<n_e>_{dia}T_{eo}} \quad , \tag{14}$$

where $< >_V$ denotes an average over the plasma volume. With the assumption of toroidal symmetry, the plasma thermal energy is written as

$$W_p = 3f<n_e>_{dia}kT_{eo}V \quad . \tag{15}$$

The form factor, for various assumed distributions, can be used to estimate W_p. The form factor reduces to unity for the case in which $T_e = T_i$, $n_e = n_i$, and the T_e and n_e distributions are uniform. It is worth noting that f can be greater than unity for $T_i > T_e$ or for hollow profiles.

B. Power Loss and Energy Containment Time

To estimate the power loss from ZT-40M, the power balance equation is used:

$$P_{in} = P_p + P_F + P_L \quad , \tag{16}$$

where P_{in} is the power input to the plasma volume, $P_p = dW_p/dt$ is the rate of increase of the plasma energy, and P_F is the power going into the magnetic field.

After substitution for P_L in Eq. (12), the energy containment time becomes

$$\tau_E = \frac{W_p}{P_{in} - P_p - P_F} \quad . \tag{17}$$

For a steady state, the plasma and field energies are constant so that P_p and P_F are zero, $P_{in} = P_L$, and τ_E reduces to W_p/P_{in}.

In the time-dependent case, the quantity W_p is evaluated by inserting Thomson-scattering and interferometer data into Eq. (15) for T_{eo} and $<n_e>_{dia}$. The value of P_p is evaluated by passing a spline fit through the shot-averaged $T_{eo}(t)$ and $<n_e>_{dia}(t)$ data and differentiating with respect to time.

The power input is computed as $V_\phi I_\phi + V_\theta I_\theta$. The voltages V_ϕ and V_θ are obtained from the toroidal-voltage and toroidal-flux loops, respectively, and the plasma current I_ϕ is measured with the Rogowski coil. The quantity I_θ is given by $(2\pi R B_{\phi w})/\mu_o$, where R is the major radius of the torus and $B_{\phi w}$ is the toroidal magnetic field measured with the extended pickup coil outside the liner. Both I_ϕ and I_θ are corrected to account for the contribution of the liner current.

Lacking internal magnetic field measurements, one can use the MBFM described in the previous section to estimate the field energy. The values of λ_o and of the transition radius r_t are chosen to fit to the external field data.[19] The power P_F going to the magnetic energy is then obtained by smoothing, fitting, and differentiating the field energy obtained from the model.

Inserting the quantities determined above into Eq. (17) gives the energy containment times τ_E reported below. Since P_p is small compared to $P_{in} - P_F$ during flat-top current operation, τ_E very nearly scales directly with the form factor f.

C. Poloidal Beta

The poloidal beta is calculated from

$$\beta_p = \frac{2}{3} \frac{W_p/V}{B_{\theta w}^2/2\mu_o} \quad , \tag{18}$$

where $B_{\theta w}$ is deduced from I_ϕ, and W_p is given by Eq. (15). This yields

$$\beta_p = 2f \frac{<n_e>_{dia} kT_{eo}}{B_{\theta w}^2/2\mu_o} \quad . \tag{19}$$

D. Results

The foregoing analysis has been applied to the data of Phases I through III. The results of Phases I and II are presented here and the Phase III results are reported in Section VIII. The calculated time-dependent curves for τ_E/f and β_p/f are shown in Figs. 19 and 20. There is an uncertainty in the magnitude and time dependence of the actual τ_E and β_p, since f might have varied with time and with the flat-top value of the toroidal current. This emphasizes the need for radial distribution measurements to determine the plasma and field energies more reliably.

More data were taken at fixed times in the discharge than during time scans of T_{eo}. One can use the density, temperature, and resistance measurements at 5 ms to predict τ_E/f and β_p/f scalings with the flat-top I_ϕ current. According to Figs. 12 and 17, $<n_e>_{dia}T_{eo}$ is approximately proportional to I_ϕ^2 at 60 to 120 kA, and $R_T \cong V_\phi/I_\phi$ is proportional to $I_\phi^{-0.85}$. The steady-state formula $\tau_E = W_p/W_{in} = W_p/(I_\phi V_\phi)$ then yields $\tau_E \propto I_\phi^{0.85}$ and $\beta_p \cong$ constant.

The results of Fig. 21 are in general agreement with these predictions. For higher currents, τ_E/f and β_p/f depart from this scaling. Figure 22 shows corresponding results at 10 ms.

The error bars in Figs. 21 and 22 represent the uncertainties in the $<n_e>_{dia}$ and T_{eo} measurements. The actual scalings of τ_E and β_p are, again, uncertain because of the unknown scaling of the form factor f. In fact, the scaling of both quantities could be more favorable at the higher current if f scaled suitably with I_ϕ. This would require T_i to increase faster than T_e and/or require increasingly flatter or hollow $<n_e>_{dia}T_{eo}$ profiles as the current increases. Increased values of T_i/T_e might result from increased turbulent heating at the higher values of the discharge current.

In conclusion, the values of τ_E/f and β_p/f appear to be roughly constant over the flat-topped portion of the discharges studied. If one assumes a constant f, the scalings of τ_E and β_p appear to be acceptable in the 60- to 120-kA range. The reason for the apparent deterioration in the scaling at a higher current is not known. It is suspected that it results from the increased plasma-wall interaction at higher currents.[20] This interaction may be associated with field errors caused by the ports and gaps in the toroidal shell. Alternatively, the drop in the scaling may reflect an increase in f with current, as discussed above.

E. Form Factor

The significance of the form factor f in the interpretation of the containment time and poloidal β scalings has been stressed in the previous paragraphs. Because of the lack of data on the electron temperature distribution and on the ion density and temperature, one cannot ascertain how f changed with the toroidal current or with time during the study.

Information is, however, available on one of the components of the form factor, namely the electron density distribution. Measurements made with the multichord IR interferometer at discharge times of up to 3 ms indicated a broadening of the density profile as the discharge current was increased. The results presented below indicate that the broadening persisted at later times in the discharges.

The profile information comes from comparisons of off-axis FIR-interferometer data and of on-axis Thomson-scattering density readings with the two-color-interferometer measurements of $\langle n_e \rangle_{dia}$. To help characterize the broadening, a density peaking factor p_n is defined as

$$p_n \equiv \frac{n_{eo}}{\langle n_e \rangle_{dia}} \quad , \tag{20}$$

where n_{eo} is the electron density on axis.

The FIR-interferometer measurements were performed during Phase I(b) at an outward distance of 12.4 cm from the minor axis of the discharge. Normalizing the data to the two-color measurements and assuming an electron density distribution of the form given by Eq. (1), one obtains the peaking factors represented by the open circles in Fig. 23. The time in the discharge is 5 ms.

A direct determination of the density peaking factor, using the ratio of the Thomson-scattering over the two-color-interferometer readings, gives the result indicated by the solid circles in the same figure. The arbitrary scale of these measurements has been adjusted to approximate the FIR result in the 120- to 180-kA range. The data were taken at 5 ms during a Phase II current scan.

The FIR result is more sensitive to the discharge current than the Thomson-scattering result. The apparent discrepancy may be due to the simple model chosen for the density distribution. A comparison of the Thomson-scattering, two-color-interferometer, and multichord-interferometer measurements was performed during Phase IV. The discharge current was varied between 60 and 180 kA and the time in the discharge was 2.5 ms. Good agreement was found between the three measurements. Also, the peaking factor determined by Thomson scattering varied more strongly with current at this early time than it does in Fig. 23.

The observed trend of p_n should have a favorable effect on the scalings of ℓ_i and β_p. The improvement depends, evidently, on the unknown behavior of the other plasma parameters. If one assumes, as an exercise, $n_e = n_i$, $T_e = T_i$, and uniform temperature distributions, then the FIR result leads to a form factor increase of the order of 14% in the interval of 120 to 180 kA.

VII. IMPURITY LEVEL, PARTICLE LOSS RATE, AND RECYCLING

The results reported in this section were obtained during Phases I(b) and II.

A. Radiation from Low-Z Impurities

Measurements of low-Z impurities were made with the Johns Hopkins 0.4-m VUV spectrometer. A detailed description of the instrument may be found in Ref. 9. The diagnostic had a useful wavelength range extending from 40 to 125 nm, with a possible resolution of 0.1 nm. To ensure coverage of the entire line radiation and to facilitate wavelength tuning, the instrumental width was set to 0.3 nm. Detector output levels of 10^{-8}, 10^{-7} and 10^{-6} A were available simultaneously, further facilitating data collection. The spectrometer viewed a horizontal diameter with a numerical aperture of approximately f/100. The absolute calibration of the instrument was checked at Johns Hopkins before installation on ZT-40M.

Species examined in the study were OIV, OV, OVI, CIII, NIV, NiIII and DI, with the wavelengths continuously cycled during ZT-40M operations. Shot-to-shot reproducibility is typically ± 30%, and no long-term drifts are evident in the Phase I(b) data.

The concentrations of low-Z impurities are determined at the time of peak emission for each species. Data from the six-chord array of QUV/V spectrometers are used at the same discharge time to ascertain the radial emission profile $P(r)$. The ion density at the minor axis is then determined by means of the relation

$$n_{io} = \frac{4\pi B}{2n_{eo}Qf\int P(r)dr} \quad , \tag{21}$$

where B is the line-integrated brightness measured with the VUV spectrometer; Q is the excitation cross section; and f, in this case, is the fractional abundance of the measured species. It is concluded that, at these early times, the impurity concentrations are 1% oxygen, 0.1% nitrogen and 0.02% carbon. These are ± 50% estimates, given the reproducibility and uncertainties in the calibrations.

Limited access and high plasma temperatures prevented the measurement of the emission profiles at later times in the discharge. Therefore, only the brightnesses of these resonance transitions are examined at 3 and 5 ms. The data are averaged at each current level, and the standard deviations are computed. The results at 3 ms are shown in Figs. 24(a) and (b). They demonstrate that, within the reproducibility of the data, the brightness of the lines examined is independent of the toroidal current. The chord-averaged density is a slowly increasing function of current so that, ignoring profile effects, there may have been a small reduction in the fraction of light impurities at higher currents. Indeed, since there is evidence that the electron density profile was wider at higher currents (Section VI), and because the species examined are expected

to have resided in the outer half of the plasma, a reduction in low-Z impurity concentrations can be inferred at higher currents.

Acquiring data on emissions from higher ionization states of low-Z impurities and on emissions from higher states of metal impurities was postponed, pending the installation of a grazing-incidence spectrometer. It should be noted that at the typical conditions of ZT-40M, line radiation from low-Z impurities is only a small fraction of the input energy; at comparable concentrations, high-Z materials could radiate a significant fraction of the input power. Their contribution to bremsstrahlung would also be much larger.

B. Recycling of Deuterium

A set of four absolutely calibrated compact D_α monitors was used to ascertain the recycling rates of deuterium and, hence, the particle containment time. Each monitor consisted of an EMI 9798B photomultiplier tube, filtered by a 1-nm FWHM interference filter centered at 656 nm, the wavelength of the D_α line. Light entered the system through a fiberoptics bundle with a diameter of 0.25 in. and a collection angle limited to 1.7 deg. The sensitivity of these monitors was periodically calibrated with a quartz lamp.

For the present calculation, the readings of the three monitors which did not view a limiter (enhanced emission had been observed at the limiter locations) are averaged, and the result is used to compute the photon flux at each current level. The photon flux is related to the ionization rate by using the atomic physics data of Johnson and Hinnov.[21] It is assumed that ionization took place in the region where the electron temperature exceeded 10 eV and where the electron density was less than or equal to 10^{13} cm^{-3}. The equation

$$\frac{d\langle n_e\rangle_{dia}}{dt} = -\frac{\langle n_e\rangle_{dia}}{\langle \tau_p\rangle_{dia}} + \sum (ionization\ rates) \qquad (22)$$

is then solved to find the diameter-averaged particle containment time $\langle \tau_p\rangle_{dia}$. Note that no attempt is made to determine the spatial resolution of this containment time. Rather, the particle containment time is derived from the diameter-averaged electron density and the diameter-averaged emission of photons. Thus, the confinement of the plasma center might have been better than is indicated here, and that at the edge might have been worse.

Particle containment times obtained as described above are shown in Table I. They show values of about 1 ms independent of time at 4 to 10 ms. A modest improvement is noted in going from 60 to 120 kA (this may be due to profile effects). There is no change from 120 to 180 kA, but there is a decrease at 240 kA. This latter trend is a consequence of averaging the photon fluxes. At 240 kA, the local photon flux was often many times higher at one D_α monitor than it was at the others. Deleting such anomalous local recycling doubles the derived containment time.

TABLE I. Diameter-Averaged Particle Containment Time

I_ϕ (kA)	$<\tau_p>_{dia}$ (ms) at 4 ms	at 7 ms	at 10 ms
60	0.7	0.6	0.5
120	1.0	1.2	1.3
180	1.0	1.1	1.1
240	0.6	0.6	0.6
240[a]	1.3	1.3	1.4

[a] After deletion of anomalously high local recycling events.

The extent of locally anomalous recycling is shown in Fig. 25. The traces show the averages and the standard deviations of all the D_α data used. These locally enhanced emissions of deuterium radiation may also be indicative of enhanced plasma-wall interaction and potential wall-damaging events at the higher currents.

A further check on the particle containment time is obtained from the electron density data. Starting at an initial time t_i, the volume-averaged density $<n_e>_V$ measured with the multichord IR interferometer is fitted during a short time interval by an expression of the form:

$$<n_e>_V(t) = <n_{ef}>_V + (<n_e>_V(t_i) - <n_{ef}>_V)\ e^{-(t-t_i)/\tau_p} \quad . \tag{23}$$

The final density $<n_{ef}>_V$ and the volume-averaged particle containment time τ_p are adjustable parameters. For t_i = 1.4 to 3 ms during a 120-kA discharge, this computation gives values of τ_p ranging from 0.33 to 1.4 ms. These numbers are comparable to those obtained from the spectroscopic data.

C. Total Radiated Power

The total power loss from the plasma was measured with the bolometer probe. This diagnostic consisted of a thin platinum foil, which was heated by the energy flux from the plasma. The temperature rise in the foil was then measured with a time constant of 0.4 ms.[10] Under the assumption that the plasma radiative energy loss was uniform over the boundary of the plasma, the foil temperature rise is translated into plasma radiative energy loss or, after differentiation, into plasma radiative power loss. The ratio of this power loss to the total power input to the plasma volume at 5 ms is then plotted as a function of current.

The data are presented in Fig. 26. It is noted that the total radiative power loss detected by the bolometer, $P_{bolometer}$, is about 50% of the total input power P_{in} at the lowest currents, falling

to 20% at the highest current. Equivalently, the power received by the bolometer is not very different at the different currents examined, with the exception of the 60-kA case. Again, profile effects have been ignored in these data, although the sensitivity of the results to assumed (reasonable) profiles is small.

VIII. OPERATION WITHOUT POLOIDAL LIMITERS

The four poloidal graphite limiters were removed after Phase II, and wall protection was then provided by graphite sleeves inserted in selected access ports. Some of the measurements made during the first two phases of operation were repeated during Phase III to identify possible changes in the performance of the facility. The measurements described in this section were carried out under the standard mode of operation. The chosen variations of the deuterium fill pressures and of the parameter Θ during this phase are shown in Figs. 27 and 28. Note that the fill pressure was slightly lower at 180 kA than it was during Phases I and II, and Θ was generally lower by 2% to 3%.

Current scans of the diameter-averaged electron density and central electron temperature are shown in Figs. 29 and 30. The time in the discharge is 5 ms, and the data are again plotted as functions of the toroidal current at the time of the measurement. The data represented by the open circles were acquired 2 weeks after the operation was resumed without poloidal limiters. The data represented by the solid symbols were obtained a week later during a Thomson-scattering run.

The electron density was lower and the electron temperature higher during the second run, an effect similar to the differences observed between Phases I and II. Wall condition improved between the two runs, as demonstrated by the measurement of the OV impurity radiation shown in Fig. 31. The OV line brightness, displayed as a function of shot number, decreased by a factor of 2 between the two runs. The improvement may have proceeded more rapidly than during the earlier phases because of the milder perturbation of the vacuum environment caused by the removal rather than the installation of limiters.

The products of the Phase III diameter-averaged electron densities and central electron temperatures are plotted in Fig. 32. Whereas the early and late sets of density and temperature data differ, the products of the two parameters overlap. As shown in the next section, the data also agree with the previous results of Phases I and II.

The toroidal voltages observed during the second set of measurements were lower than those obtained during the first set, and the effective resistivities on axis are correspondingly lower. Such a trend is not surprising in view of the higher electron temperatures recorded during the second set of measurements. The effect, however, is only slightly apparent in the results, shown in Fig. 33, of discharges for which electron temperature measurements were made.

The toroidal voltages measured during Phase III were mostly lower than the voltages observed during Phases I and II, and the Phase III resistivities were, therefore, lower also. A comparison of the results obtained with and without poloidal limiters is presented in the next section. Some of the difference may have been caused by the small differences in the discharge conditions noted earlier.

Plots of the poloidal beta and energy containment time achieved during Phase III are shown in Figs. 34(a) and (b), as functions of the nominal toroidal current. The data are calculated at 5 ms in the discharges under the assumptions described in Section VI. Based on the behaviors of $<n_e>_{dia}T_{eo}$ and of the toroidal voltage, one would expect the poloidal beta to have remained approximately the same and the energy containment time to have increased. A comparison with Fig. 21 indicates a longer containment time at 120 kA. Differences among the other data points are within the error bars.

In summary, the removal of the poloidal limiters had only a small, if any, effect on the scaling of the products $<n_e>_{dia}T_{eo}$ and on the poloidal beta. The effective resistivity on axis was lower, and the energy containment time at 120 kA was higher. Part of these effects may have been due to small differences in the discharge conditions.

IX. OTHER SCALINGS

The scaling results presented in this section were obtained at higher fill pressures or at earlier times in the discharges and, therefore, involve a departure from the standard mode of operation. The discussion is limited to the scalings of the electron density, temperature, product $<n_e>_{dia}T_{eo}$, and effective resistivity on axis.

A. Pressure Scans

During Phases II and III, experiments were performed in which the fill pressure was varied over the entire usable pressure range. The pressure scans were carried out at nominal toroidal currents of 60 to 180 kA. They involved fewer discharges (as few as two in some cases) than the measurements performed under standard conditions. The results obtained on the basis of these measurements must, therefore, be considered tentative.

Varying the fill pressure had the effect illustrated by the 120-kA Phase II results of Fig. 35. The initial toroidal current peak was followed by a dip that became more pronounced as the fill pressure was increased. The current was restored to its initial peak value at a later time in the discharge by adjusting the power crowbar settings. Thus, the current waveform no longer satisfied the quasi-steady-state conditions. The rate of change of the current at the time of the measurements, however, remained slow compared to the particle and energy containment times.

The diameter-averaged electron density, central electron temperature, and products of the two parameters obtained at 5 ms under these conditions are shown in Figs. 36 through 38. The electron density and temperature each show a significant change with fill pressure. The variation of the product $<n_e>_{dia}T_{eo}$, on the other hand, is less pronounced. If one takes into account the decrease of the instantaneous toroidal current with increasing fill pressure, the variation of $<n_e>_{dia}T_{eo}$ becomes even less significant.

During Phase III, pressure scans were performed at nominal toroidal currents of 60 to 180 kA. These experiments were carried out immediately before and after the first current scan mentioned in Section VIII. Figure 39 shows the ranges of fill pressures covered during this survey. The lowest value of each range approached the pressures used under standard conditions. The effective resistivities on axis, obtained at 5 ms in the discharges, are plotted in Fig. 40. They vary by as much as 40% at a given nominal toroidal current. This demonstrates that the chosen variation of the fill pressure with the discharge current reported in the previous Sections had a strong influence on the scaling of the resistivity. Note, however, that similar resistivity scalings are achieved with the experiment running at either the high or the low end of the usable pressure ranges.

The diameter-averaged electron densities and products $<n_e>_{dia}T_{eo}$ recorded at the highest pressure settings of the pressure scans are represented by the open circles in Figs. 41 and 42. A comparison of the electron density with the densities recorded under standard discharge conditions reveals a 44% increase at 120 kA. The difference between the high-density products $<n_e>_{dia}T_{eo}$ of Fig. 42 and the standard results of Fig. 32 is small at high discharge currents. However, the product is larger than the standard result achieved at the low end of the current scale.

The effective resistivities on axis obtained under these high fill pressure conditions are represented by the open circles in Fig. 43. They are generally higher than the standard Phase III resistivities of Fig. 33.

B. Early Discharge Time

High-density results such as those achieved at high fill pressures were also obtained under standard discharge conditions when the measurements were performed at early times in the discharges. The electron density and temperature then varied more rapidly than at 5 ms, but the variations were still slow compared to the containment times. Measurements of the diameter-averaged electron density, the product $<n_e>_{dia}T_{eo}$, and the effective resistivity on axis, taken at 3 ms in standard discharges, are represented by the solid circles in Figs. 41 through 43.

When comparing these early-time results with the high-pressure measurements, the electron densities are found to track each other well over the entire current range. The agreement is fortuitous in that the outcome would have been different had the early-time measurement been

performed at another time in the discharges. The early-time electron temperatures (not shown) are somewhat higher than the high fill pressure temperatures. This effect is reflected in the slightly higher values of $\langle n_e \rangle_{dia} T_{eo}$ at 90 through 180 kA. The two resistivities on axis are essentially the same in spite of this difference.

The results displayed in Figs. 41 through 43 can be viewed as a tentative evaluation of the high-density scaling of ZT-40M. A least-squares fit through the combined $\langle n_e \rangle_{dia} T_{eo}$ data suggests a scaling proportional to $I_\phi^{1.24}$ over the full range of toroidal currents. The scaling still shows a tendency to weaken as the current is increased, but the effect is less pronounced than in the standard mode of operation. The effective resistivity is higher because of the generally lower electron temperatures. The combined resistivity data scale as $I_\phi^{-0.69}$, a performance similar to the standard result.

C. Comparison With Standard Results

Figure 44 shows a superposition of the Phases I and II, the Phase III, and the high-density Phase III measurements of $\langle n_e \rangle_{dia} T_{eo}$. These data were individually shown in Figs. 12, 32, and 42. The error bars have been omitted for clarity. As previously noted (for example, when comparing Phase I to Phase II results) the experiment displays a strong tendency to maintain the same products at given discharge currents. This is particularly true at discharge currents exceeding 90 kA. At low current, the high-density products are somewhat larger than the standard results.

Another composite plot, Fig. 45, compares the effective resistivities on axis under the same three operating conditions. These data were previously shown in Figs. 15, 33, and 43. As previously stated, the Phase III resistivities are generally lower than the Phase I and Phase II resistivities, and the high-density results are higher than the standard Phase III results. The resistivities obtained in the three modes of operation show similar scalings.

D. Constant I_ϕ/N_e

The scaling results can, presumably, be made less sensitive to the chosen mode of operation by imposing a constraint on one of the plasma parameters. It has been suggested, for example, that scaling data be evaluated at a constant ratio of the toroidal current over the electron line density.[22] A glimpse at how ZT-40M would have scaled at constant I_ϕ/N_e can be gained from the data collected during the Phase III pressure scans. Because of the scarcity of these data, the results must again be viewed as tentative.

The outcome of this exercise is shown in Figs. 46 through 49. Rather than being strictly proportional to the discharge current, the available electron density data scale as I_ϕ to the power (1.06 ± 0.07), and I_ϕ/N_e falls within $(0.81 \pm 0.05) \cdot 10^{-13}$ A-m for a parabolic density distribution. Under these conditions, the central electron temperature scales as $I_\phi^{0.43}$, and the

product $\langle n_e \rangle_{dia} T_{eo}$ as $I_\phi^{1.41}$, over the 60- to 180-kA range. The slope of the density-temperature products continues to show a decline at high current, but the effect is weaker than in the standard mode of operation. The effective resistivity on axis scales as $I_\phi^{-0.73}$, a feature similar to the previous results. Combining the scalings of Figs. 47 and 49 one deduces that the effective resistivity scales approximately as $T_{eo}^{-1.6}$.

X. CONCLUSIONS

ZT-40M scaling measurements have been carried out at nominal discharge currents ranging from 60 to 240 kA. The scaling data were acquired at a fixed time in the discharges while the plasma was in a quasi-steady state. Most of the scaling measurements were performed under a standard set of discharge conditions.

Some of the measurements were affected by gradual changes in the condition of the discharge chamber. These changes have been taken into account in the interpretation of the electron density and temperature data. The products of these two parameters, which enter into the calculation of the poloidal beta and the energy containment time, are found to be relatively insensitive to these variations.

Data taken with four poloidal graphite limiters, and with the discharge chamber conditioned over an extended period of operation, give the diameter-averaged electron density $\langle n_e \rangle_{dia}$ scaling as $I_\phi^{1.31}$, the central electron temperature T_{eo} scaling as $I_\phi^{0.55}$, and the product $\langle n_e \rangle_{dia} T_{eo}$ scaling as $I_\phi^{1.95}$ at discharge currents ranging from 60 to 120 kA. The slope of $\langle n_e \rangle_{dia} T_{eo}$ decreases as the current is extended to 240 kA. Spectroscopic observations show that the falloff is accompanied by increased plasma-wall interaction.

Calculations of the effective electrical resistivity on axis and of resistivities based on energy and helicity balance produce results consistent with classical electrical resistivity enhanced by a Z_{eff}, which is attributed to impurities in the discharges, and by fluctuations associated with the dynamo effect. The effective resistivity on axis scales classically as $T_{eo}^{-1.5}$.

The poloidal beta is defined on the basis of the product $\langle n_e \rangle_{dia} T_{eo}$ and a form factor that incorporates the uncertainties associated with the density and temperature distributions and with the ratio of the electron to ion temperatures. The poloidal beta, thus normalized, is approximately constant as a function of current up to 120 kA and then falls off at higher currents. When normalized to the same form factor, the energy containment time, which also depends on the resistivity of the discharge, scales approximately as $I_\phi^{0.85}$ at 60 to 120 kA and then levels off at higher currents. The scalings of the actual poloidal beta and the actual energy containment time are stronger if the undetermined values of T_i/T_e and/or the broadening of the radial distributions increased with current.

Measurements without poloidal limiters show similar behaviors of the electron density and temperature and give essentially the same products $<n_e>_{dia}T_{eo}$. The electrical resistivity, on the other hand, is somewhat lower in the absence of the limiters. The poloidal beta is essentially the same and the energy containment time is higher at 120 kA than with the limiters in place. Some of the differences may be attributable to slight differences in the discharge conditions.

Spectroscopy measurements, made while the facility was operated with the carbon limiters, give impurity contents of 1% oxygen, 0.1% nitrogen, and 0.02% carbon at 3 ms in the discharges. The particle containment time is estimated at 0.5 to 0.7 ms at 60 kA, and at 1.0 to 1.4 ms at higher currents. Half of the energy losses at low current to 20% of the losses at high current are attributed to radiation.

Data taken under nonstandard conditions give the following tentative results. At high electron density, $<n_e>_{dia}T_{eo}$ scales as $I_\phi^{1.24}$ from 60 to 240 kA. Data selected to give an approximately constant ratio I_ϕ/N_e scale as $I_\phi^{1.41}$ from 60 to 180 kA. At high currents, both measurements show a more moderate rise of $<n_e>_{dia}T_{eo}$ than at low currents, but the effect is less pronounced than under the standard conditions. The scalings of the effective resistivity are comparable to the standard results.

The high-density results should facilitate a comparison of the present work with the ZT-40M scaling studies performed in 1984 and 1985. These experiments encompassed measurements of round-top discharges,[23] and studies of short flat-top discharges.[24] The constant I_ϕ/N_e data should help compare the performance of ZT-40M with that of other RFP facilities.

XI. ACKNOWLEDGMENTS

The scaling team was responsible for the planning, execution and interpretation of the results of this study. Specific areas of interest to the team members were: D. A. Baker and E. J. Caramana, scaling theory and energy containment time; A. Haberstich, coordination and Thomson scattering; E. M. Little, Thomson scattering; A. R. Jacobson, interferometry; K. F. Schoenberg, plasma resistivity; K. S. Thomas, facility operation; and P. G. Weber, spectroscopy.

The section on plasma resistivity in this report was written by K. F. Schoenberg; the section on energy containment time and poloidal beta, with the exception of subsection E, by D. A. Baker; and the section on impurity level, particle loss rate and recycling by P. G. Weber. These contributions were prepared in 1983, and, although they are not contradicted by more recent results, they nevertheless reflect the more limited understanding of the ZT-40M performance at that time.

The other authors made significant contributions in the following areas: J. N. DiMarco, RFP program coordination; R. G. Watt and A. E. Schofield, facility operation; R. G. Watt,

establishment of low-current discharge conditions; R. S. Massey and C. J. Buchenauer, plasma equilibrium; C. J. Buchenauer two-color interferometry; R. M. Erickson, FIR interferometry; J. C. Ingraham, bolometry; and J. A. Phillips, plasma resistivity.

Thanks are due to J. N. Downing, who was responsible for the vacuum system and wall protection, and to R. W. Wilkins and K. A. Klare who provided the control and data acquisition systems. The technical support given by N. L. Salazar, P. A. Freeman, and M. D. Pacheco in the operation of the facility is gratefully acknowledged.

The preparation of this report was encouraged by R. E. Siemon and benefitted from valuable comments by D. A. Baker, C. J. Buchenauer, E. J. Caramana, J. N. Downing, R. M. Erickson, J. C. Ingraham, J. A. Phillips, K. F. Schoenberg, R. G. Watt, and P. G. Weber. The authors are indebted to K. A. Klare and J. A. Phillips for helping with the retrieval of the original data.

This work was performed under the auspices of the U. S. Department of Energy.

XII. REFERENCES

1. A. Haberstich, D. A. Baker, E. J. Caramana, A. R. Jacobson, E. M. Little, J. A. Phillips, K. F. Schoenberg, K. S. Thomas, and P. G. Weber, "Temperature and Resistivity of the ZT-40M RFP With Poloidal Limiters," *Bull. Am. Phys. Soc.* **28**, 1097 (1983).

2. D. A. Baker, C. J. Buchenauer, E. J. Caramana, R. M. Erickson, A. Haberstich, A. R. Jacobson, E. M. Little, K. F. Schoenberg, K. S. Thomas, and P. G. Weber, "Density, Beta and Confinement Properties of the ZT-40M RFP With Poloidal Limiters," *Bull. Am. Phys. Soc.* **28**, 1097 (1983).

3. R. S. Massey, C. J. Buchenauer, L. C. Burkhardt, A. R. Jacobson, J. G. Melton, G. Miller, R. W. Moses, K. F. Schoenberg, and R. G. Watt, "Preliminary Equilibrium and Field Error Studies on ZT-40M," Los Alamos National Laboratory report LA-9567-MS (February 1983).

4. R. S. Massey, C. J. Buchenauer, G. Miller, and G. Barnes, "Preliminary Results from ZT-40M Using Active Feedback for Equilibrium Control," Los Alamos National Laboratory report LA-9809-MS (July 1983).

5. J. N. Downing, C. J. Buchenauer, J. C. Ingraham, R. A. Krakowski, J. A. Phillips, and R. G. Watt, *J. Nucl. Mater.* **128**, 517 (1984).

6. A. R. Jacobson, and L. J. Jolin, "Eight-Chord CO_2 Interferometer for Plasma Density Measurements on ZT-40," *Los Alamos Conference on Optics '81*, D. H. Liebenberg, Ed. (SPIE, Bellingham, Washington, 1981), Vol. 288, 269.

7. C. J. Buchenauer, "Acoustically Compensated Two-Wavelength Interferometry for Plasma Density Measurements: One-Dimensional Theory and Applications," Los Alamos National Laboratory report LA-9880-MS (February 1984).

8. R. M. Erickson, "Far-Infrared Polarimetry/Interferometry for Poloidal Magnetic Field Measurement on ZT-40M," Los Alamos National Laboratory report LA-10731-T (Thesis) (June 1986).

9. H. W. Moos, K. I. Chen, J. L. Terry, and W. G. Fastie, *Appl. Opt.* **18**, 1209 (1979).

10. G. Miller, J. C. Ingraham, and L. S. Schrank, *Rev. Sci. Instrum.* **53**, 1410 (1982).

11. J. A. Phillips, L. C. Burkhardt, A. Haberstich, R. B. Howell, J. C. Ingraham, E. M. Little, K. S. Thomas, R. G. Watt, and P. G. Weber, "ZT-40M Current Risetime Study," Los Alamos National Laboratory report LA-9717-MS (October 1983).

12. K. F. Schoenberg, R. W. Moses Jr., and R. L. Hagenson, *Phys. Fluids* **27**, 1671 (1984).

13. E. J. Caramana and D. A. Baker, *Nucl. Fusion* **24**, 423 (1984).

14. R. R. Inglis, *Rev. Mod. Phys.* **43**, 481 (1981).

15. H. K. Moffatt, Magnetic Field Generation in Electrically Conducting Fluids, (Cambridge University Press, Cambridge, MA, 1978).

16. L. Spitzer Jr., Physics of Fully Ionized Gases, (Wiley Interscience, New York, NY, 1962).

17. M. K. Bevir and J. W. Gray, in "Proceedings of the Reversed Field Pinch Theory Workshop, Los Alamos, 1980," Los Alamos National Laboratory report LA-8944-C (January 1982).

18. G. A. Wurden, "Soft X-Ray Array Results on the ZT-40M Reversed-Field Pinch," *Phys. Fluids* **27**, 551 (1984).

19. K. F. Schoenberg, R. F. Gribble, and J. A. Phillips, *Nucl. Fusion* **22**, 1433 (1982).

20. D. A. Baker, C. J. Buchenauer, L. C. Burkhardt, E. J. Caramana, J. N. DiMarco, J. N. Downing, R. M. Erickson, R. F. Gribble, A. Haberstich, R. B. Howell,

J. C. Ingraham, A. R. Jacobson, K. A. Klare, E. M. Little, R. S. Massey, J. G. Melton, G. Miller, R. W. Moses, C. P. Munson, J. A. Phillips, M. M. Pickrell, R. A. Nebel, A. E. Schofield, K. F. Schoenberg, R. G. Watt, P. G. Weber, D. M. Weldon, K. A. Werley, R. W. Wilkins, G. A. Wurden, D. D. Schnack, D. C. Baxter, A. Y. Aydemir, and D. C. Barnes, "Experimental and Theoretical Studies of the ZT-40M Reversed-Field Pinch," in Plasma Physics and Controlled Nuclear Fusion Research, 1984 (Proc. 10th Int. Conf. London, 1984), Vol. 2, IAEA, Vienna (1985) p. 439.

21. L. C. Johnson, and E. Hinnov, *J. Quant. Spectrosc. Radiat. Trans.* **13**, 333 (1973).

22. S. Ortolani and G. Rostagni, *Nucl. Instru. & Methods* **207**, 35 (1983).

23. J. A. Phillips, C. P. Munson, and G. A. Wurden, *Bull. Am. Phys. Soc.* **29**, 1403 (1984).

24. G. A. Wurden, D. M. Weldon, P. G. Weber, R. G. Watt, A. E. Schofield, M. M. Pickrell, J. A. Phillips, C. P. Munson, G. Miller, J. C. Ingraham, R. B. Howell, and C. J. Buchenauer, *Bull. Am. Phys. Soc.* **30**, 1402 (1985).

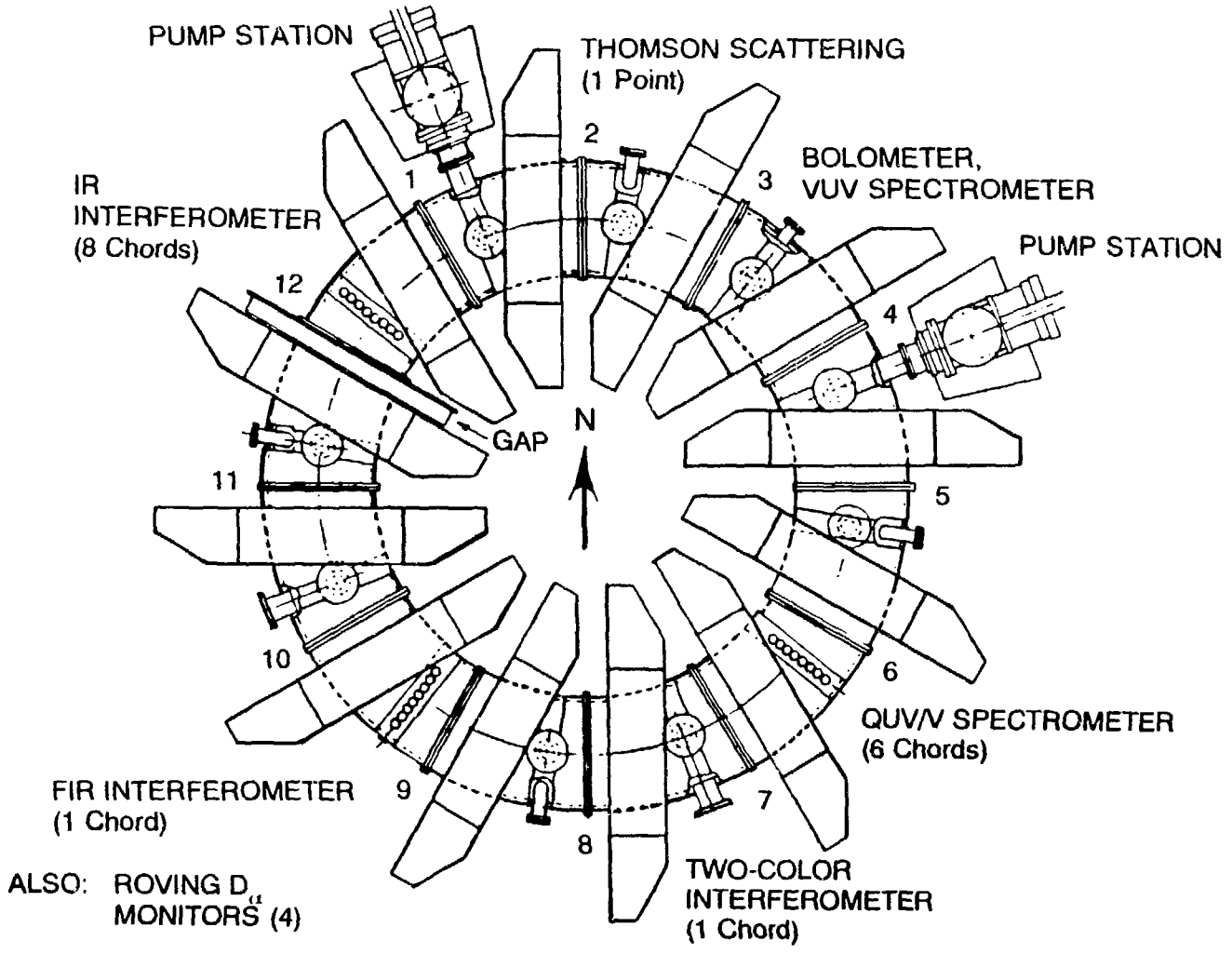

Fig. 1. Top view of ZT-40M. The diagnostics stations and plasma diagnostics used during the present study are identified.

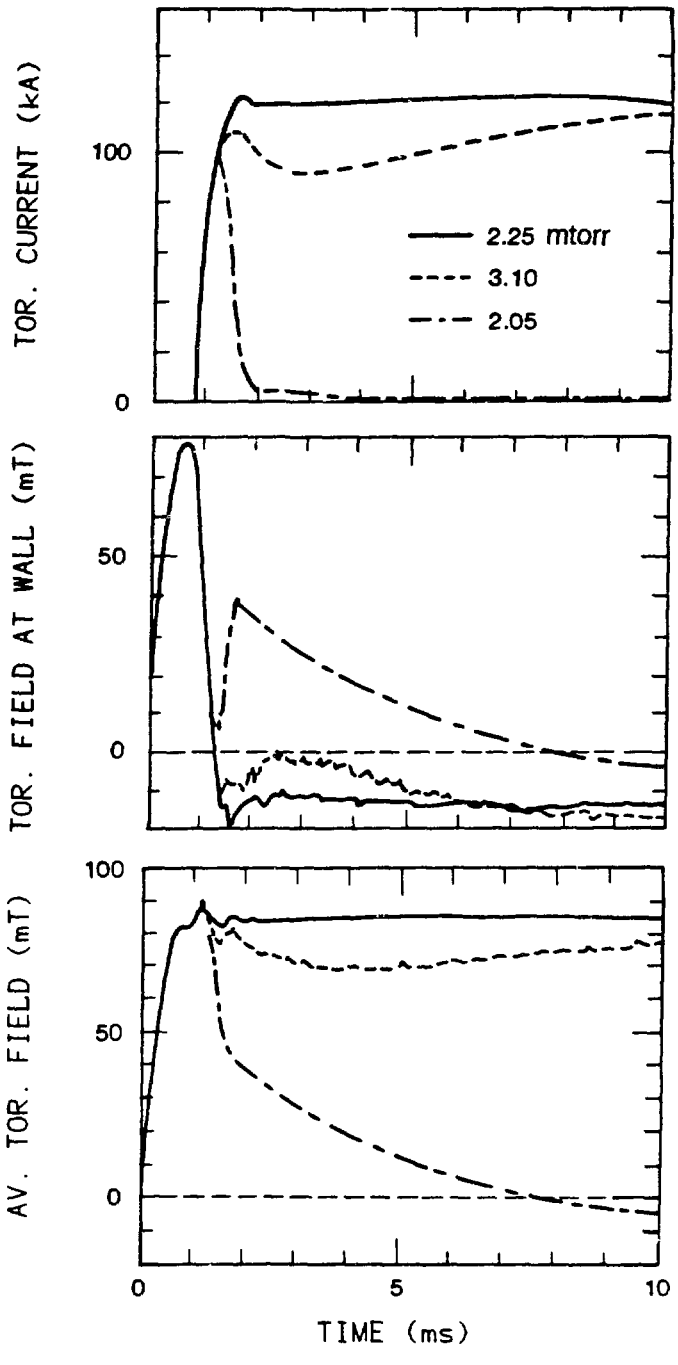

Fig. 2. Traces of three 120-kA discharges, showing the effect of extreme variations of the deuterium fill pressure.

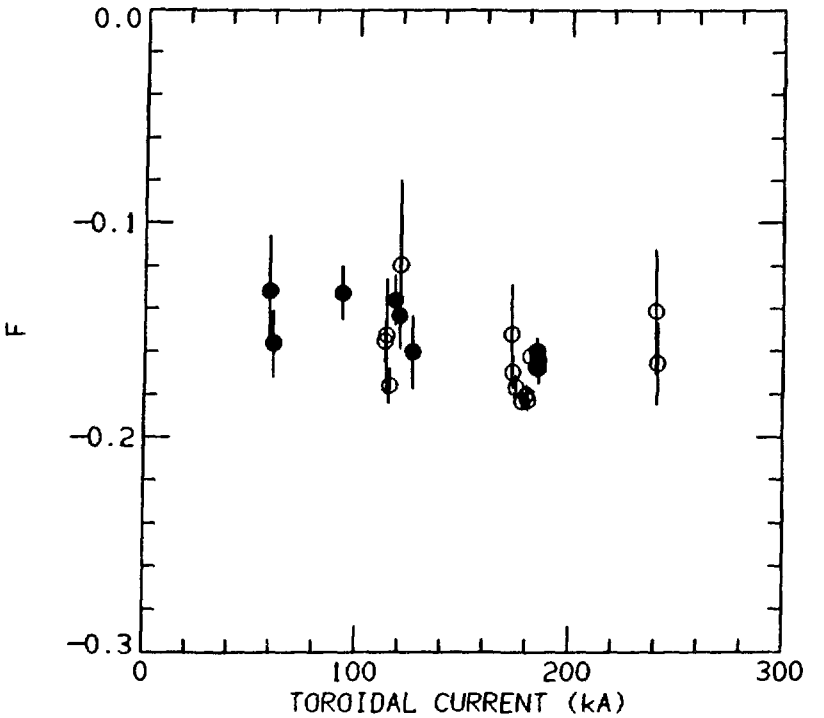

Fig. 3. Pinch parameter F vs toroidal current, measured at 5 ms during Phases I (open circles) and II (solid circles).

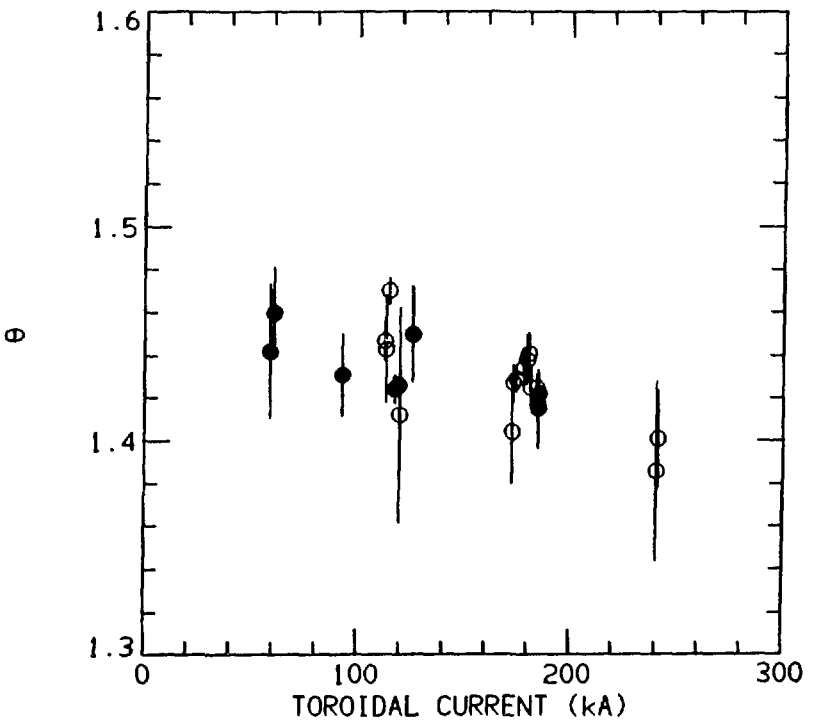

Fig. 4. Pinch parameter Θ vs toroidal current, measured at 5 ms during Phases I (open circles) and II (solid circles). Same conditions as in Fig. 3.

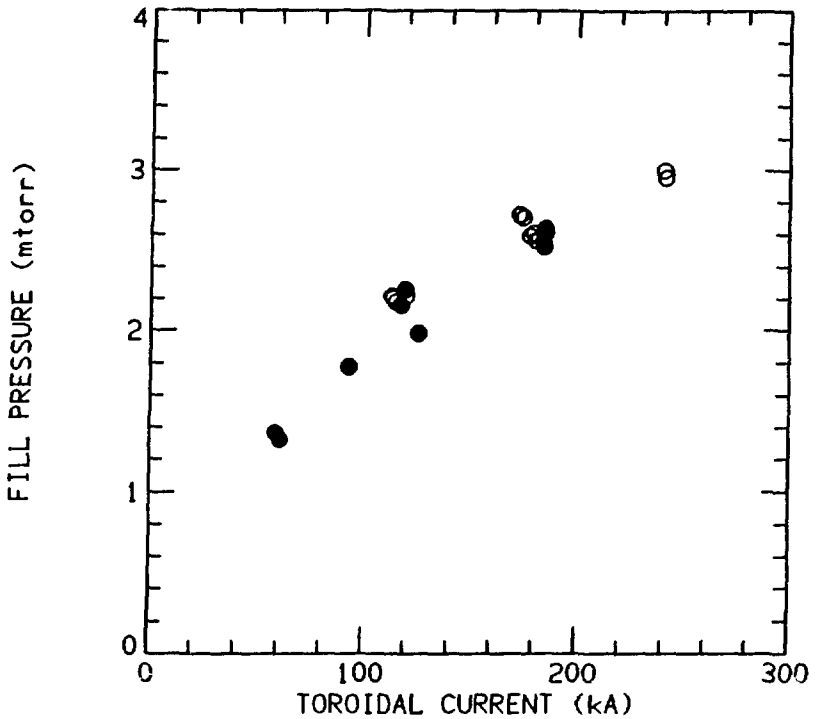

Fig. 5.. Deuterium fill pressure vs toroidal current at 5 ms, measured during Phases I (open circles) and II (solid circles). Same conditions as in Fig. 3.

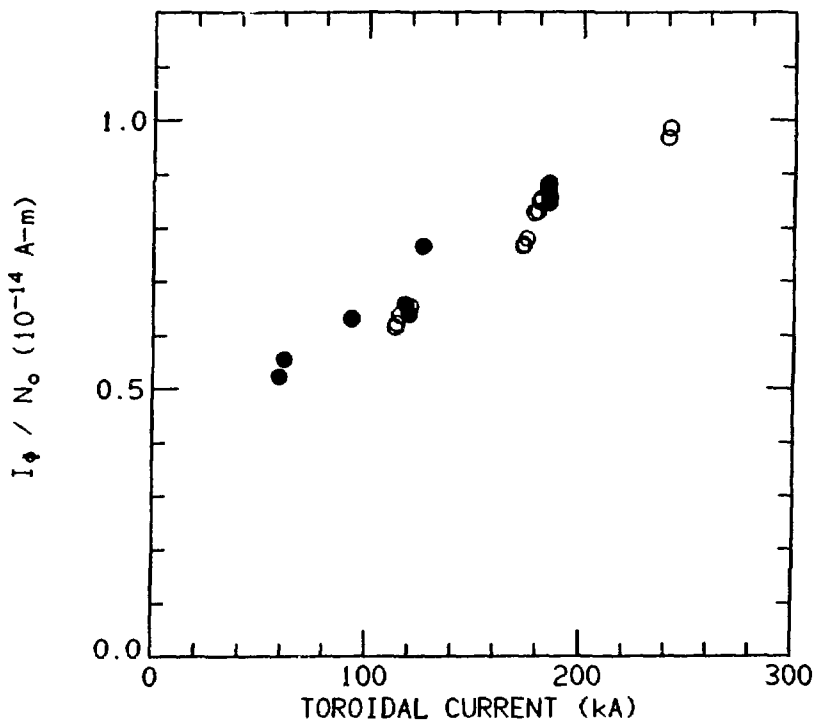

Fig. 6. Ratio of the toroidal current I_ϕ at 5 ms over the initial gas density N_o, measured during Phases I (open circles) and II (solid circles). Same conditions as in Fig. 3.

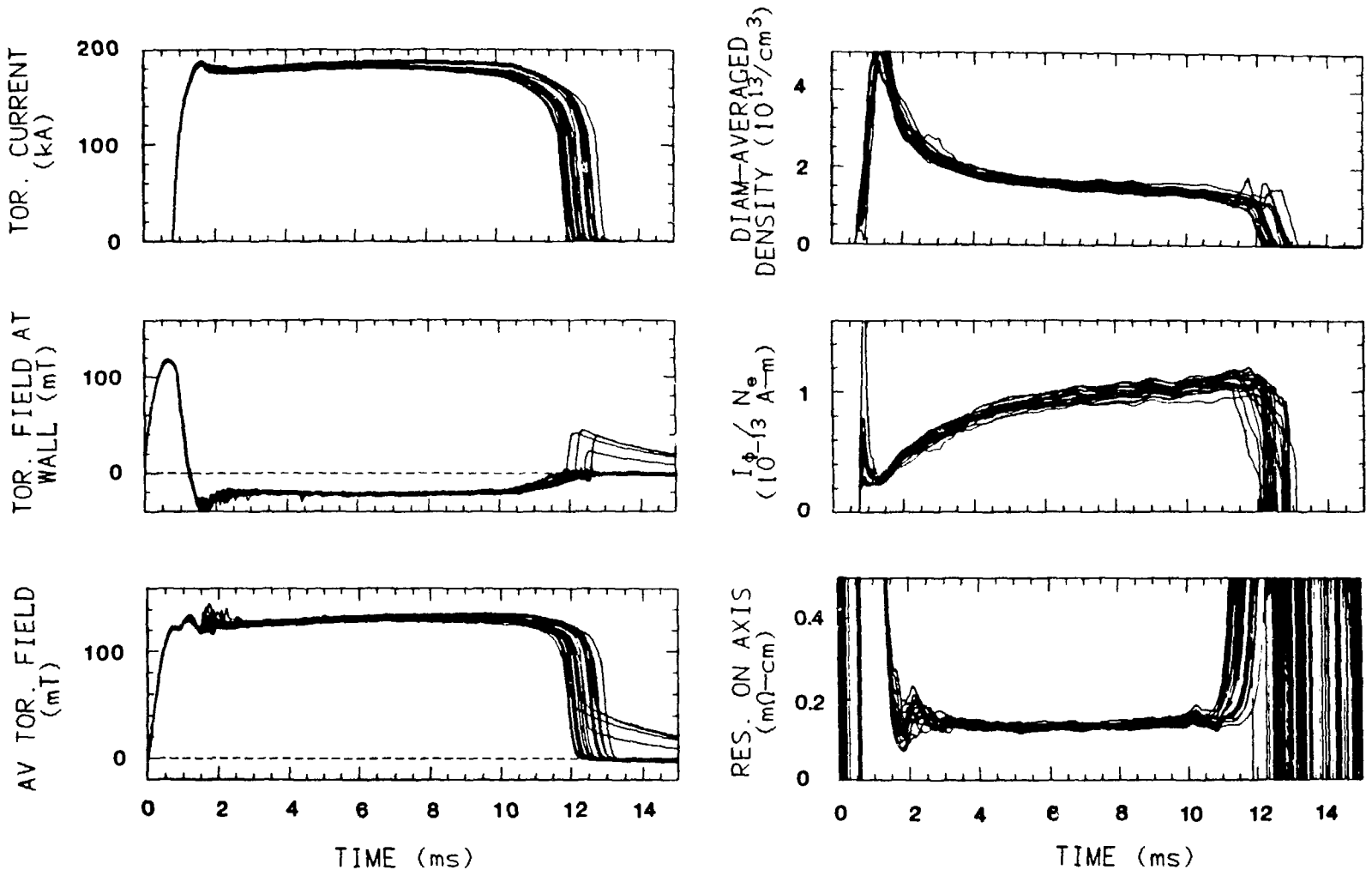

Fig. 7. Superposed traces of twenty 180-kA discharges recorded during Phase I.

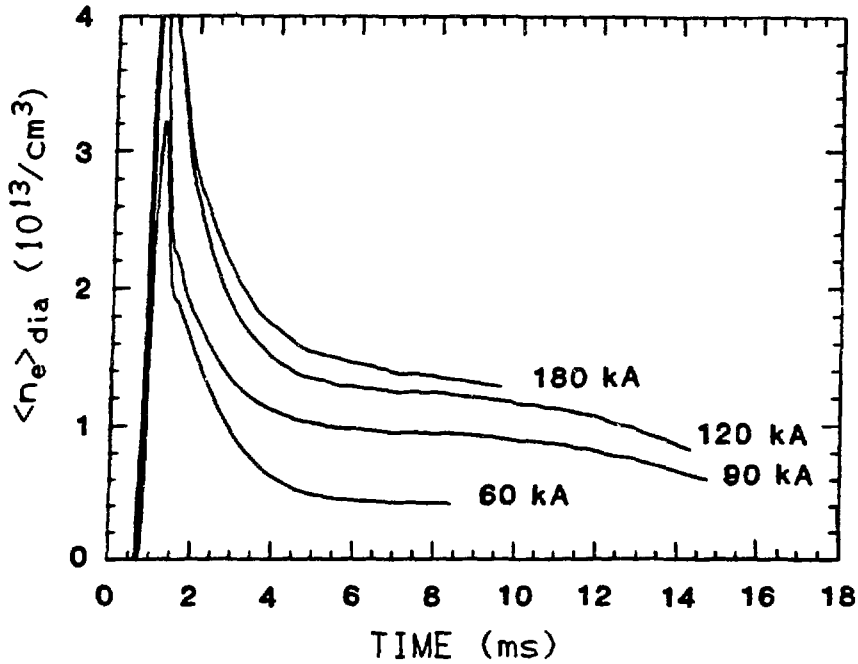

Fig. 8. Diameter-averaged electron density vs time, at nominal toroidal currents of 60, 90, 120, and 180 kA. Phase II data.

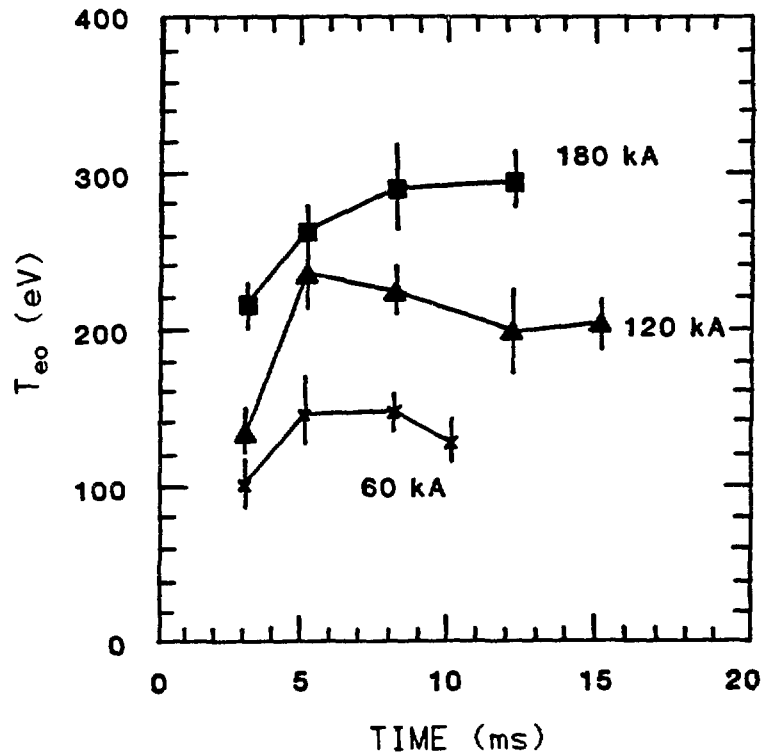

Fig. 9. Central electron temperature vs time, at nominal toroidal currents of 60, 120, and 180 kA. Phase II data.

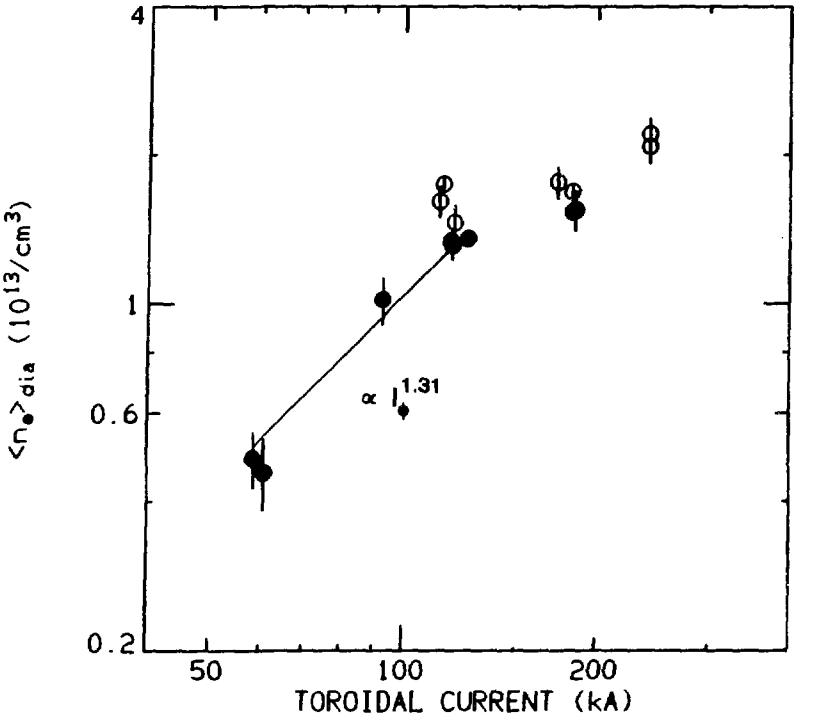

Fig. 10. Diameter-averaged electron density vs toroidal current, at 5 ms. Open circles measured during Phase I, solid circles during Phase II. Phase II data fitted over currents ranging from 60 to 120 kA.

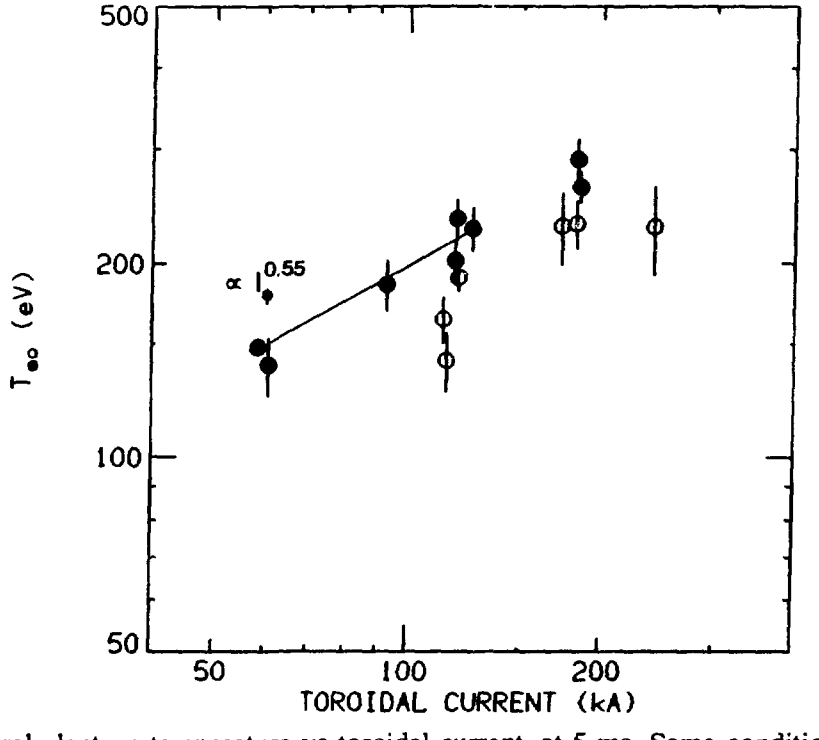

Fig. 11. Central electron temperature vs toroidal current, at 5 ms. Same conditions as in Fig. 10, with the exception of a missing data point at 240 kA. Phase II data fitted over currents ranging from 60 to 120 kA.

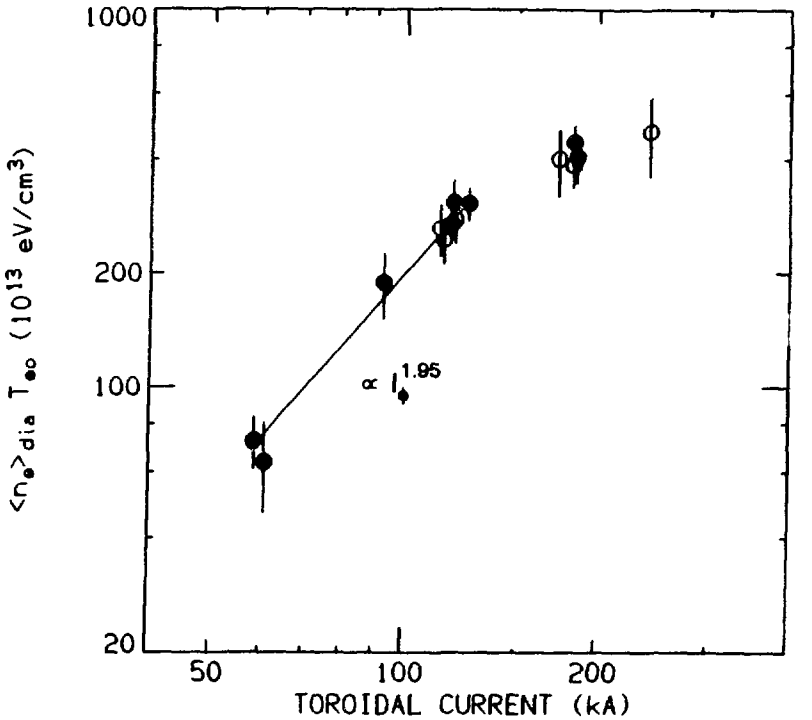

Fig. 12. Product of the diameter-averaged electron density and the central electron temperature vs toroidal current, at 5 ms. Same conditions as in Fig. 11. Phases I and II data fitted over currents ranging from 60 to 120 kA.

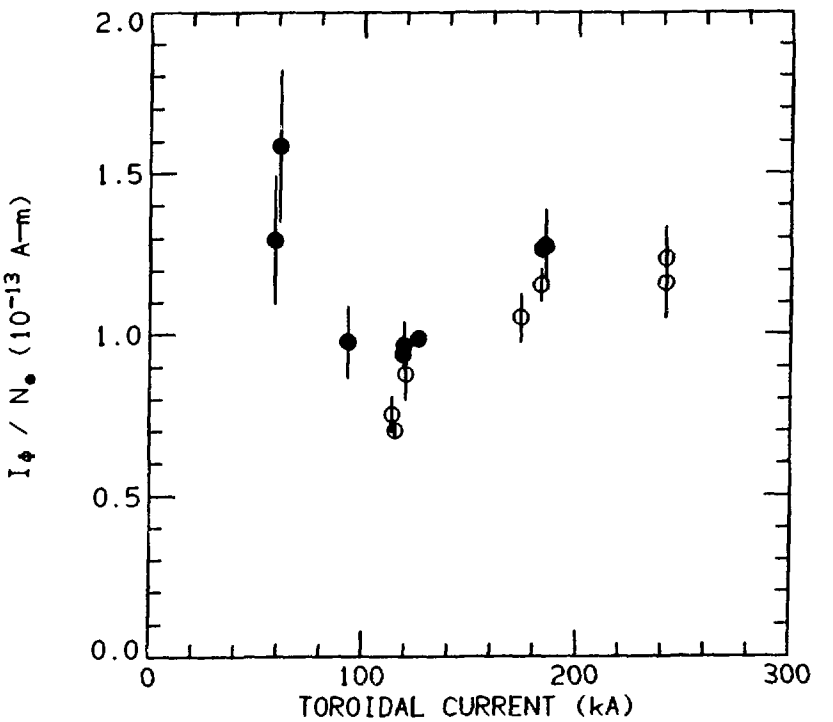

Fig. 13. Ratio of the toroidal current over the electron line density vs toroidal current, at 5 ms. The electron density distribution is assumed to be parabolic. Same Phases I and II conditions as in Fig. 10.

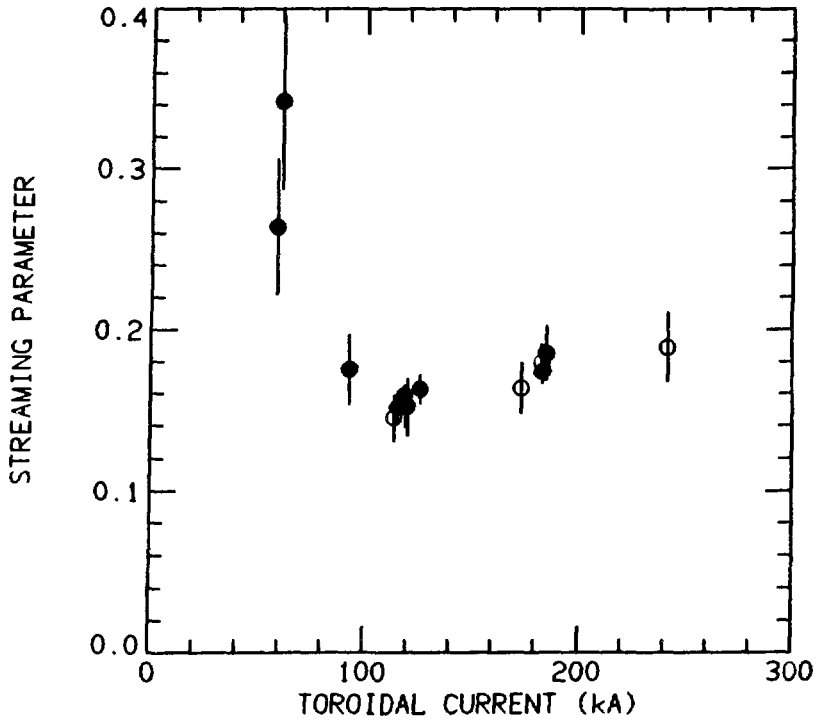

Fig. 14. Streaming parameter on axis vs toroidal current, at 5 ms. The toroidal current peaking factor is based on the modified Bessel function model. Same Phases I and II conditions as in Fig. 11.

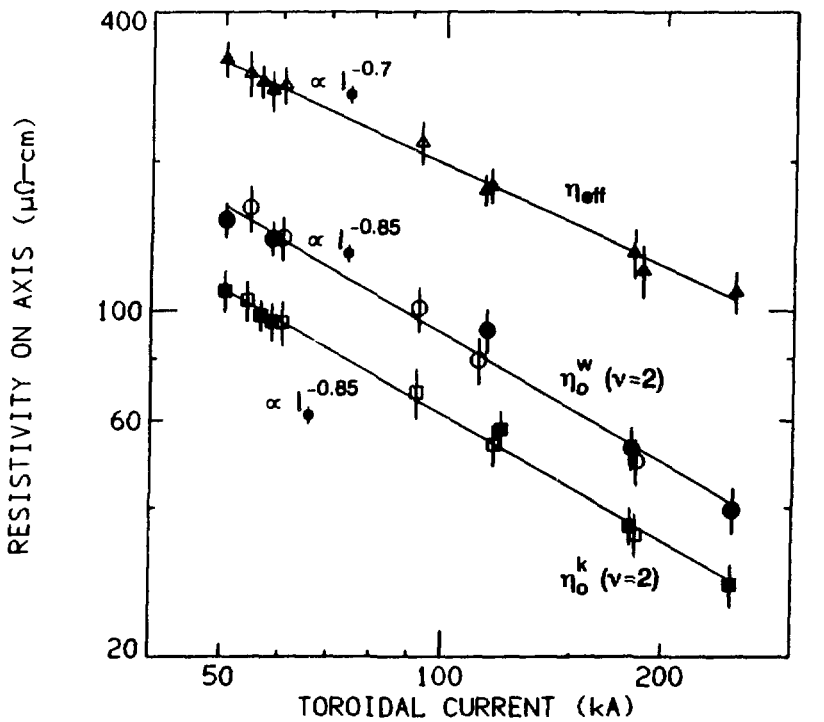

Fig. 15. Electrical resistivities η_{eff}, η_o^w, and η_o^k vs toroidal current. Phases I and II data at 5 ms.

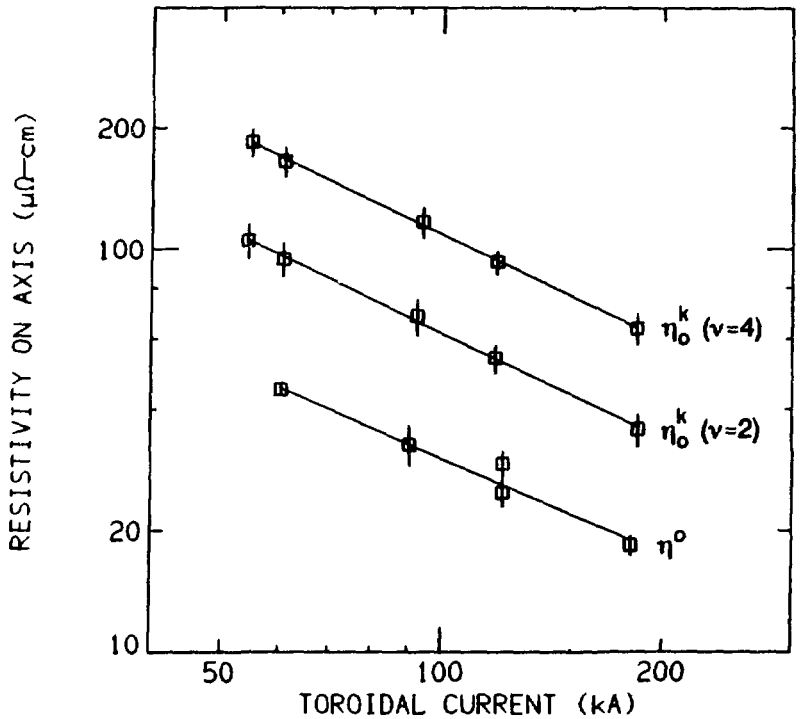

Fig. 16. Global helicity resistivities η_o^k calculated for two resistivity distributions, and Spitzer resistivity η^o derived, for $Z_{eff} = 1$, from the measured central electron temperature. Phase II data at 5 ms.

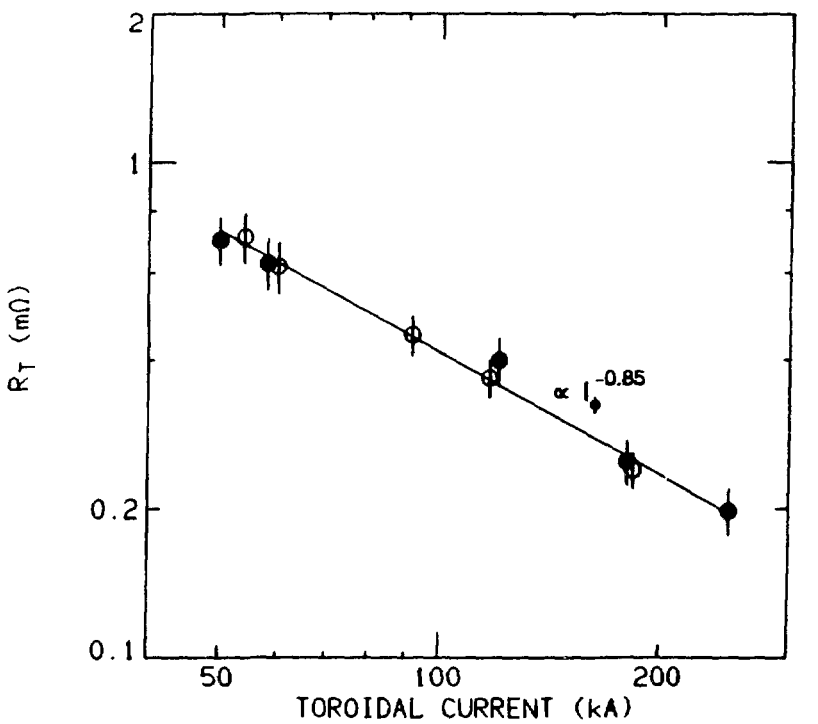

Fig. 17. Global plasma resistance R_T vs toroidal current. Phases I and II data at 5 ms.

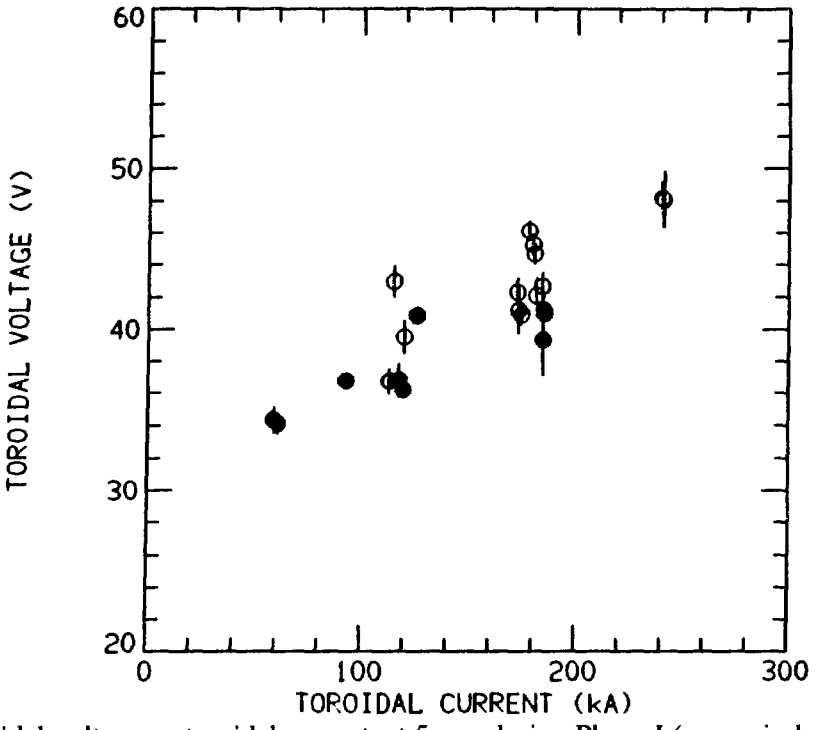

Fig. 18. Toroidal voltage vs toroidal current, at 5 ms, during Phase I (open circles) and Phase II (solid circles). Same conditions as in Fig. 3.

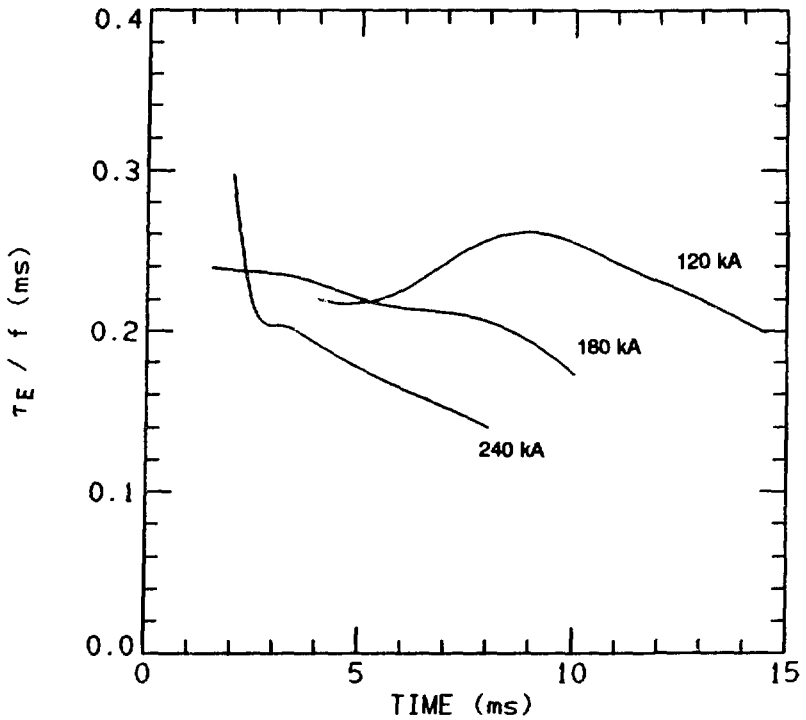

Fig. 19(a). Energy containment time, normalized to the form factor *f*, vs time. Nominal toroidal currents 120, 180, and 240 kA. Phase I data.

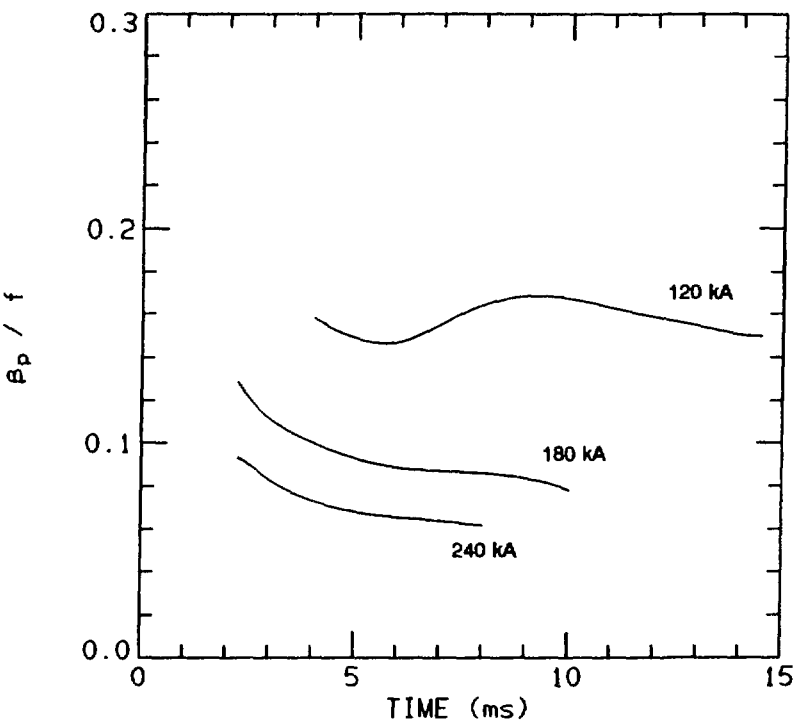

Fig. 19(b). Poloidal beta, normalized to the form factor *f*, vs time. Same conditions as in Fig. 19(a).

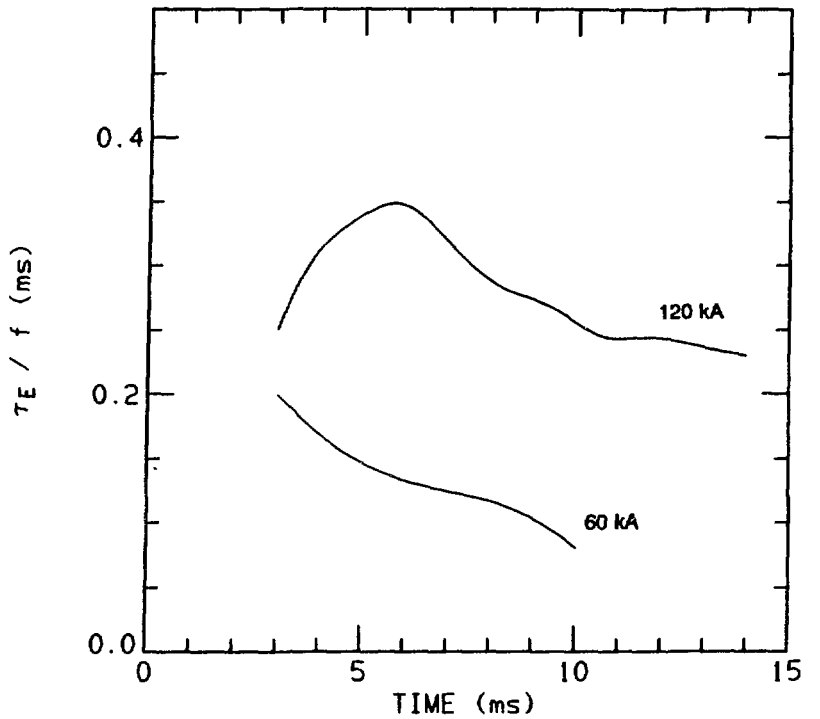

Fig. 20(a). Energy containment time, normalized to the form factor *f*, vs time. Nominal toroidal currents 60 and 120 kA. Phase II data.

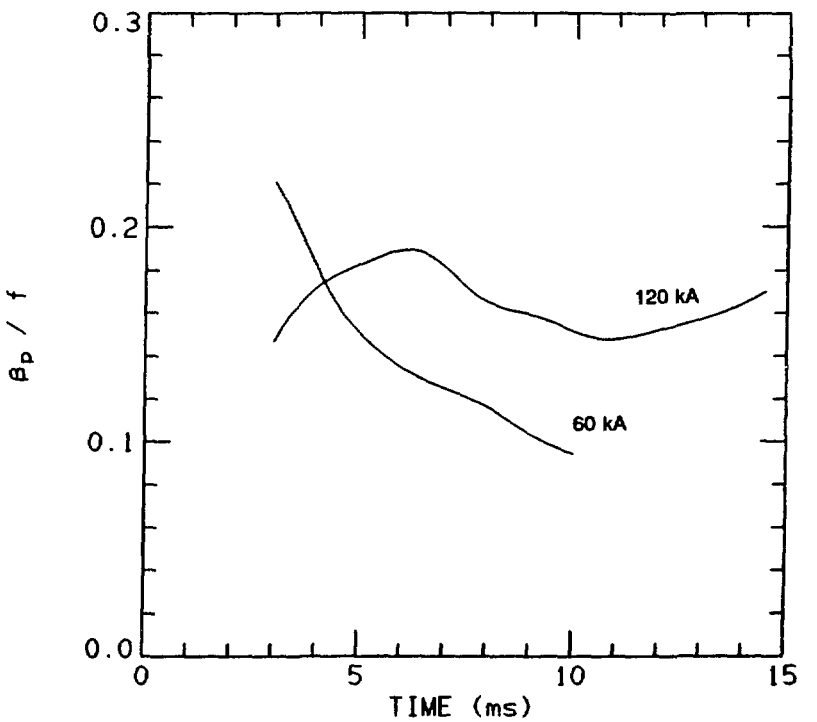

Fig. 20(b). Poloidal beta, normalized to the form factor *f*, vs time. Same conditions as in Fig. 20(a).

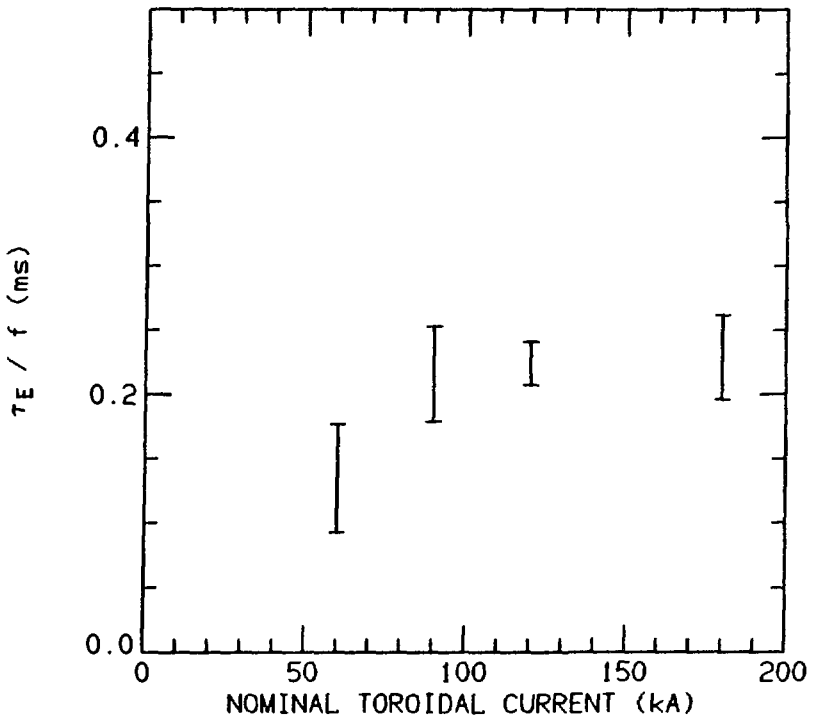

Fig. 21(a). Energy containment time, normalized to the form factor *f*, vs nominal toroidal current. Phase II data at 5 ms.

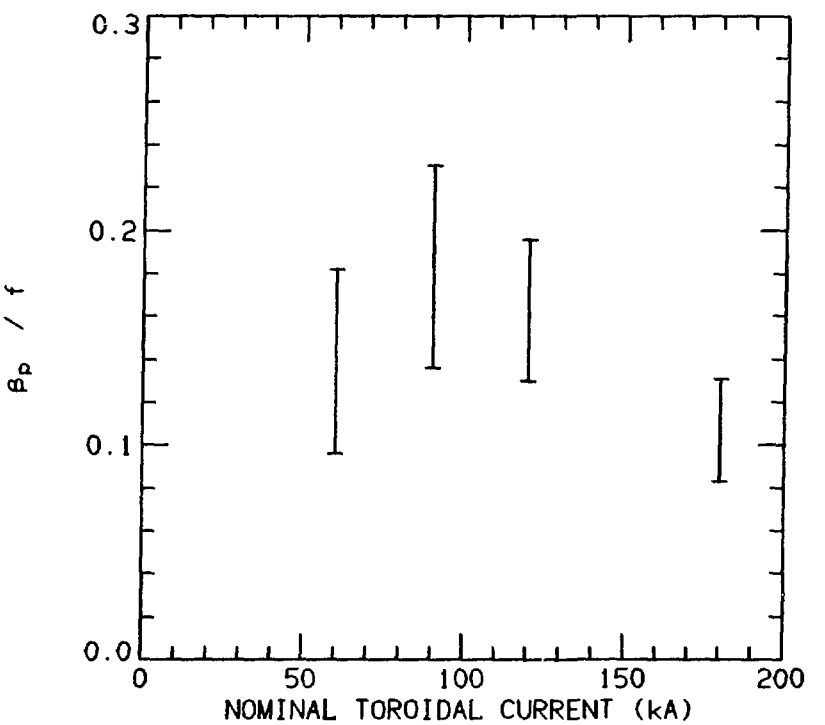

Fig. 21(b). Poloidal beta, normalized to the form factor *f*, vs nominal toroidal current. Same conditions as in Fig. 21(a).

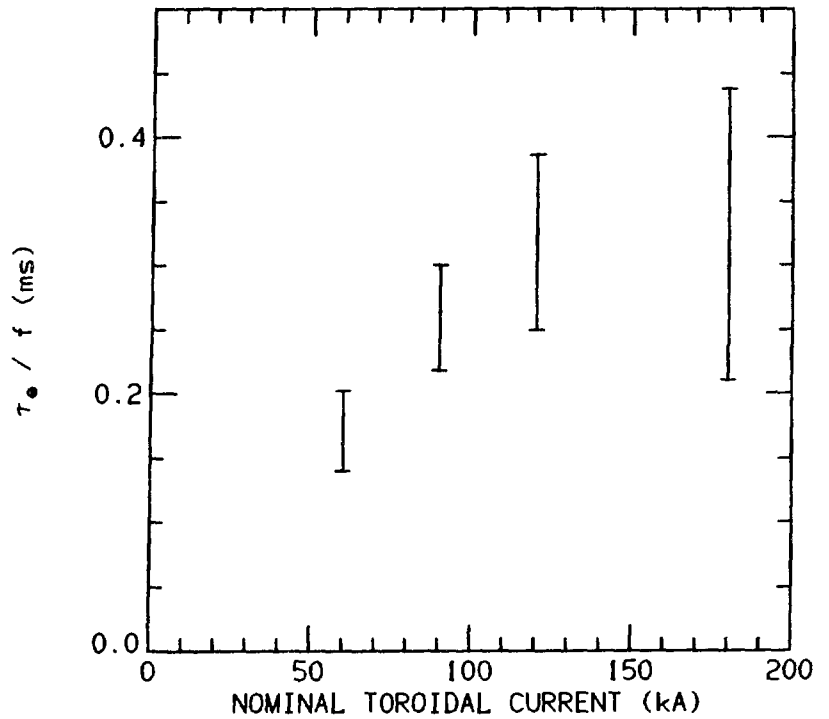

Fig. 22(a). Energy containment time, normalized to the form factor *f*, vs nominal toroidal current. Phase II data at 10 ms.

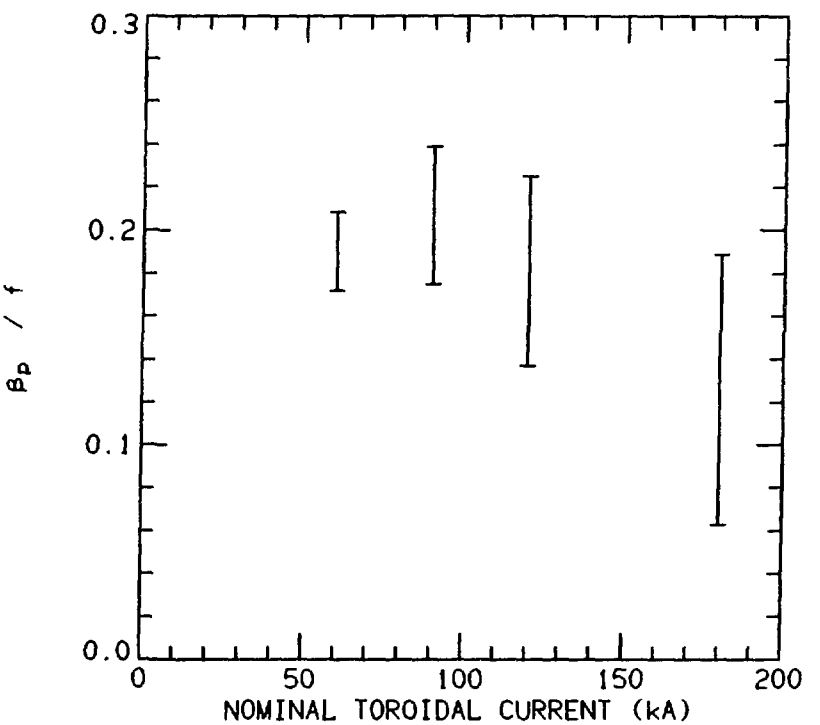

Fig. 22(b). Poloidal beta, normalized to the form factor *f*, vs nominal toroidal current. Same conditions as in Fig. 22(a).

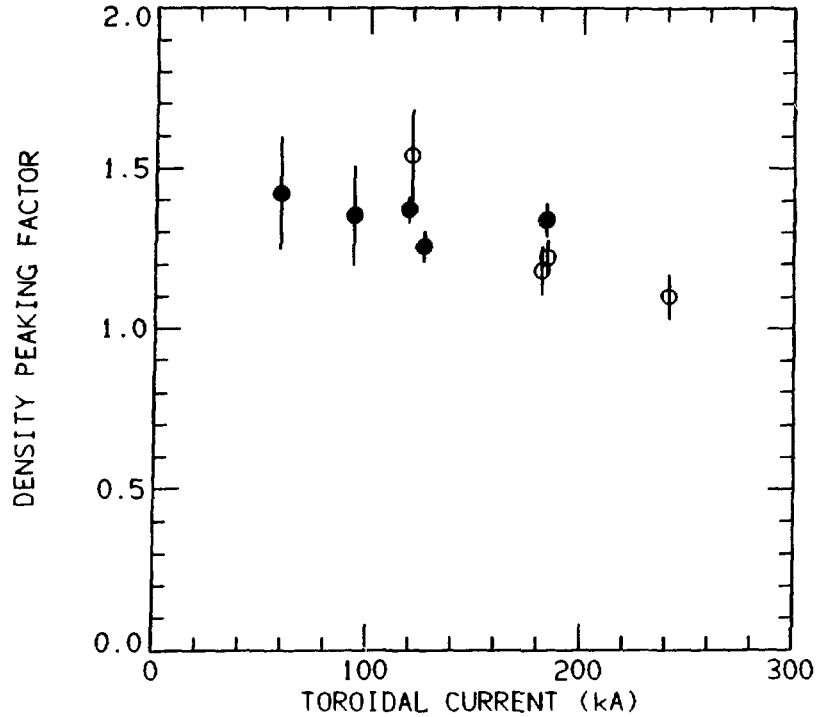

Fig. 23. Density peaking factor vs toroidal current. Open circles obtained during Phase I with off-axis FIR interferometer. Solid circles measured during Phase II with Thomson scattering (arbitrary scale). Data taken at 5 ms.

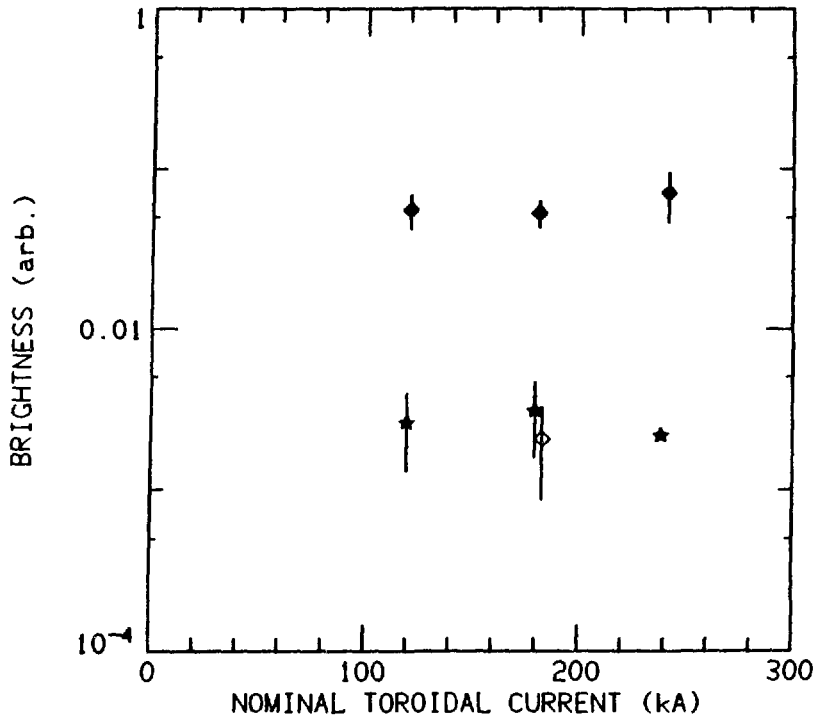

Fig. 24(a). Line-integrated brightnesses of OVI (solid diamonds), CIII (stars), and DI (open diamond) vs toroidal current. Phase I(b) data at 3 ms.

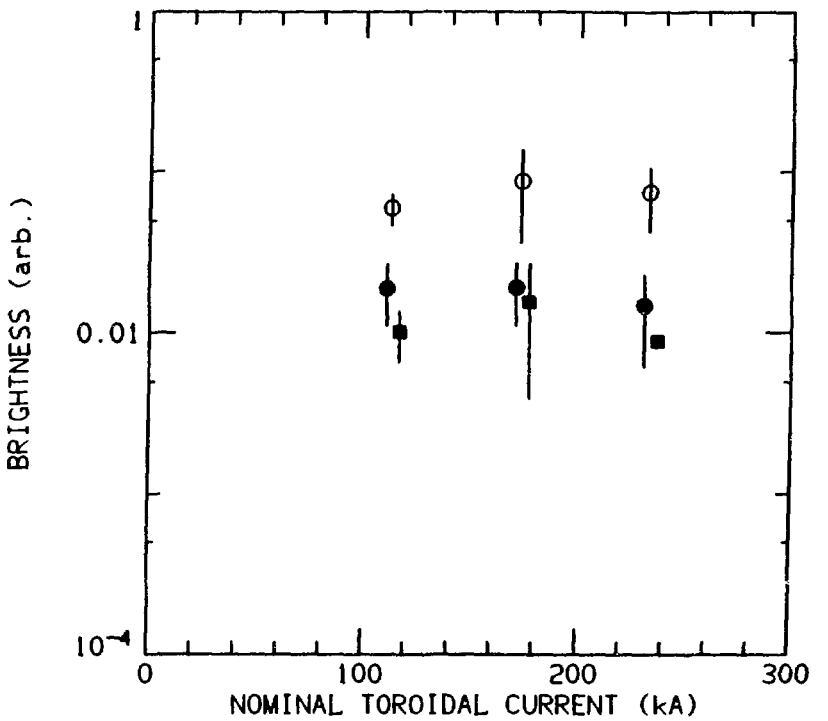

Fig. 24(b). Line-integrated brightnesses of OV (open circles), OIV (solid circles), and NIV (solid squares). Same scales and conditions as in Fig. 24(a).

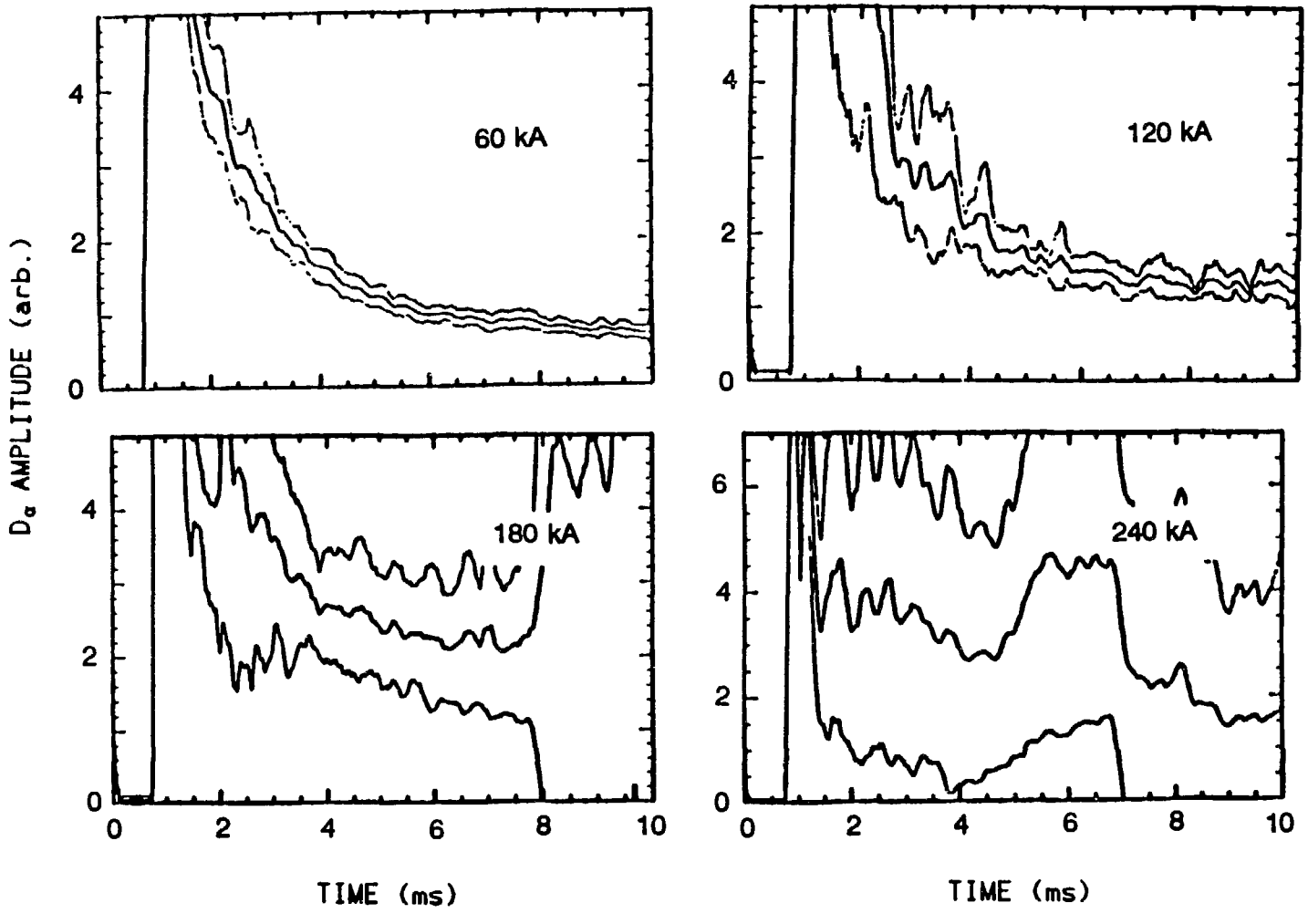

Fig. 25. Averages and averages +/- standard deviations of the D_α monitor signals used in the calculation of the particle confinement times of Table I. Phases I and II data.

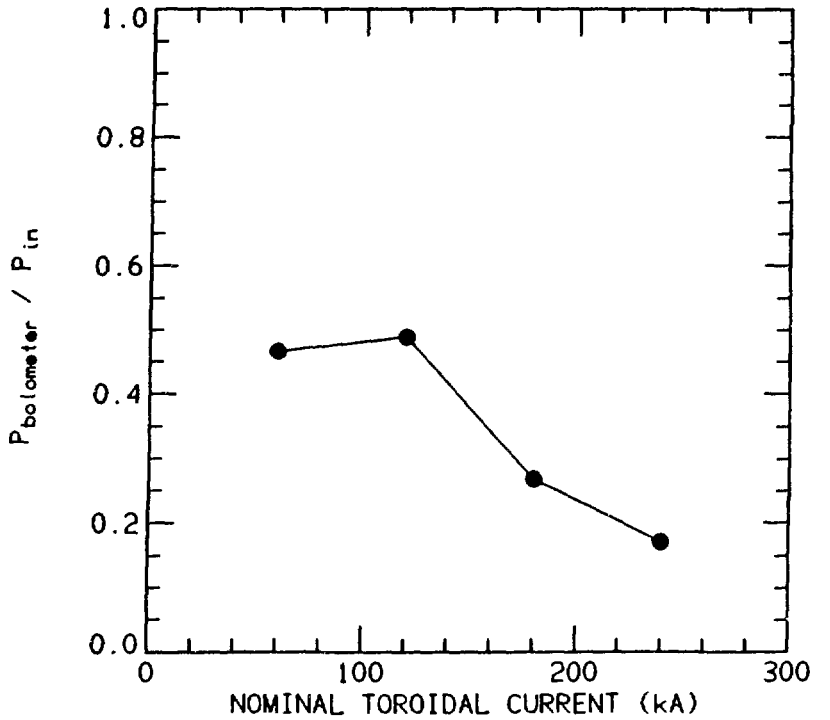

Fig. 26. Bolometer measurements of the total radiated power normalized to total power input to the discharge, at nominal toroidal currents of 60, 120, 180, and 240 kA. Phases I and II data at 5 ms.

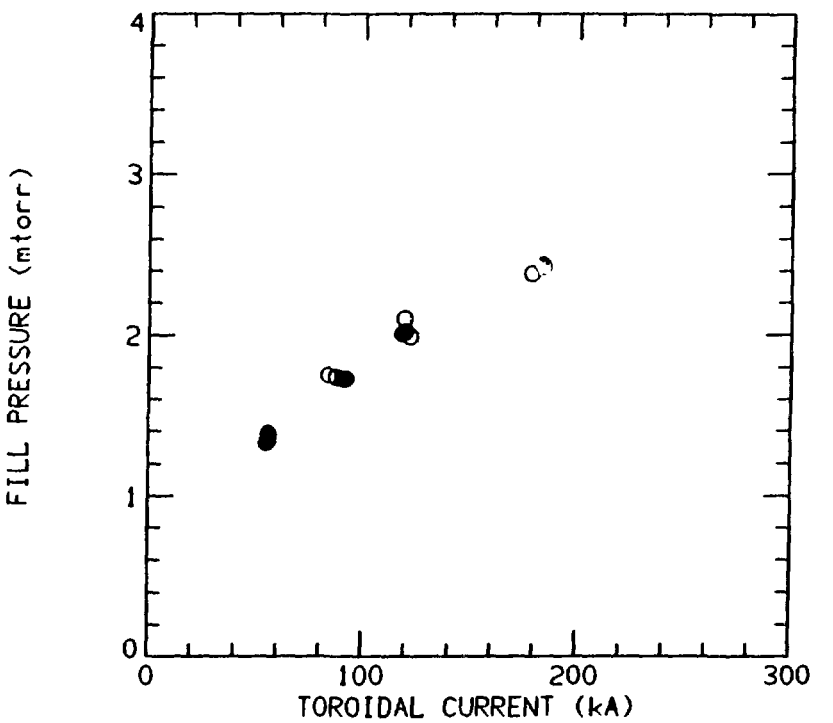

Fig. 27. Deuterium fill pressure used during Phase III, vs toroidal current at 5 ms. Open and solid circles measured 2 and 3 weeks, respectively, after the poloidal limiters were removed.

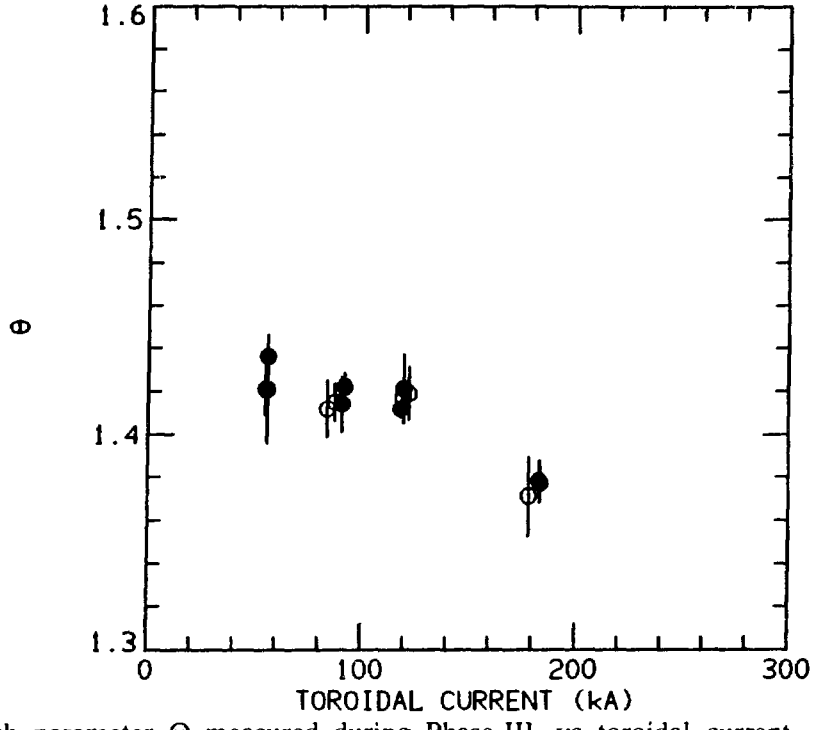

Fig. 28. Pinch parameter Θ measured during Phase III, vs toroidal current, at 5 ms. Same conditions as in Fig. 27.

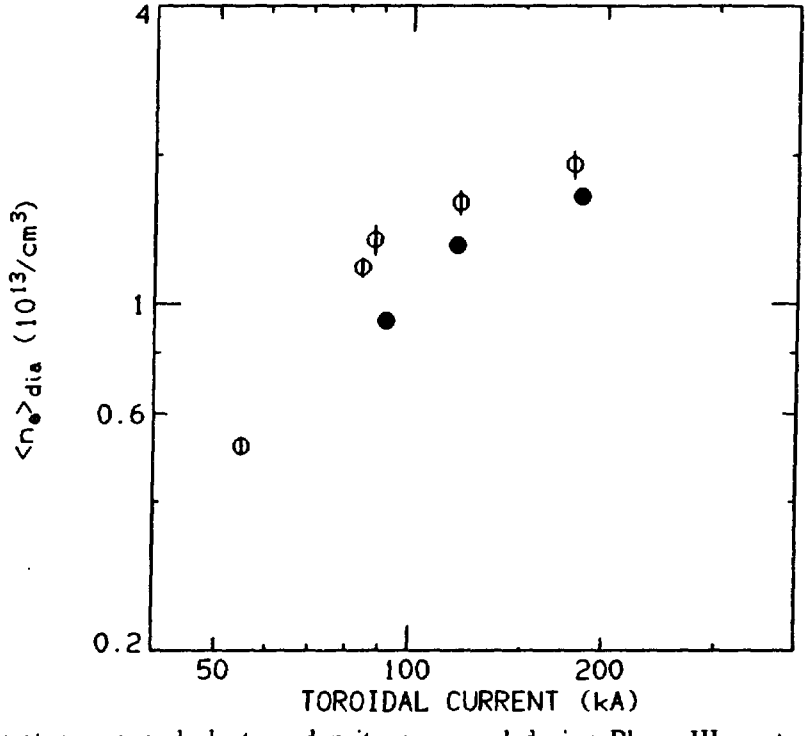

Fig. 29. Diameter-averaged electron density measured during Phase III, vs toroidal current, at 5 ms. Open and solid circles measured 2 and 3 weeks, respectively, after the poloidal limiters were removed.

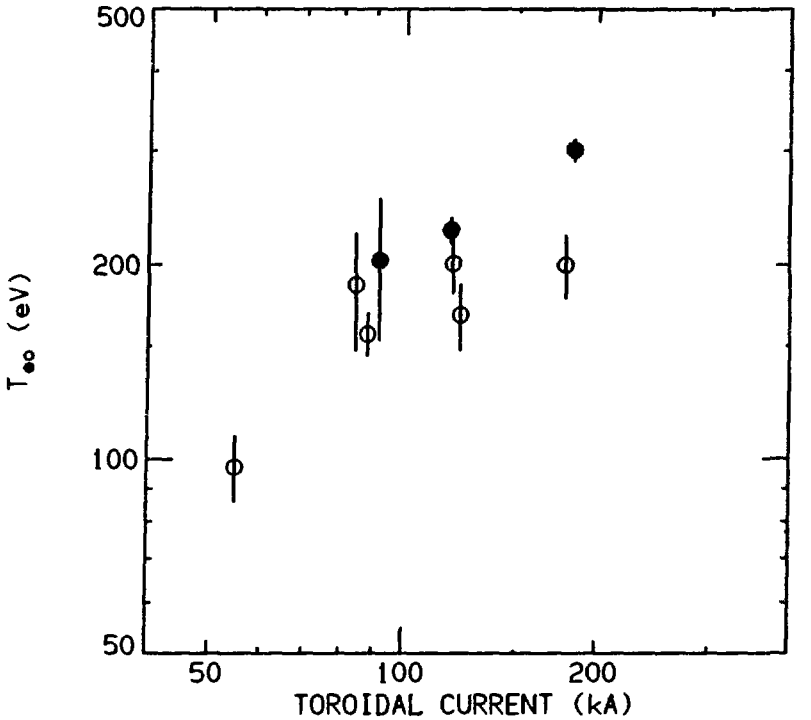

Fig. 30. Central electron temperature vs toroidal current, at 5 ms. Same conditions as in Fig. 29.

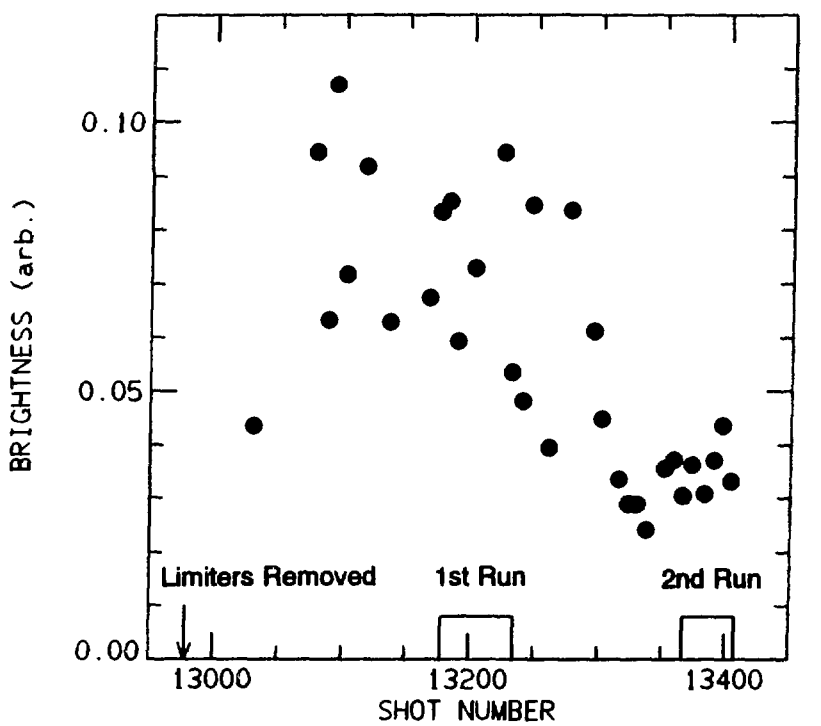

Fig. 31. Brightness of the OV line vs shot number during Phase III.

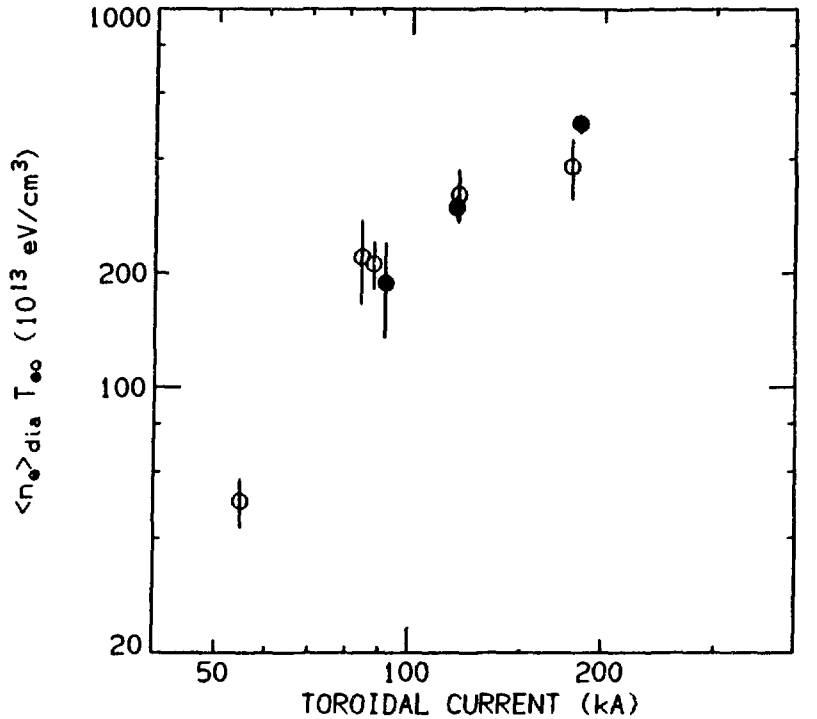

Fig. 32. Product of the diameter-averaged electron density and the central electron temperature vs toroidal current, at 5 ms. Same conditions as in Fig. 29.

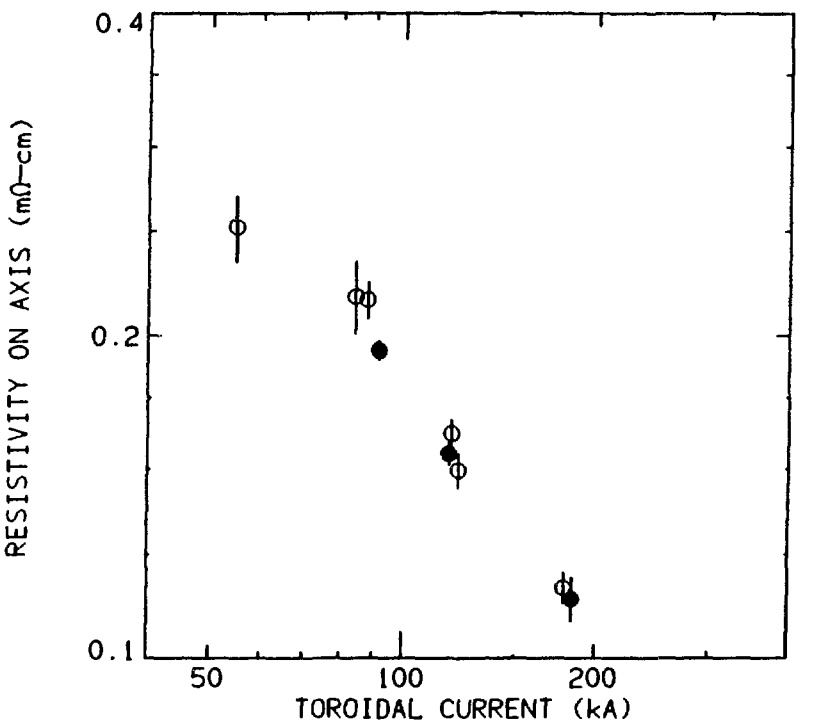

Fig. 33. Effective resistivity on axis during Phase III vs toroidal current, at 5 ms. Same conditions as in Fig. 29.

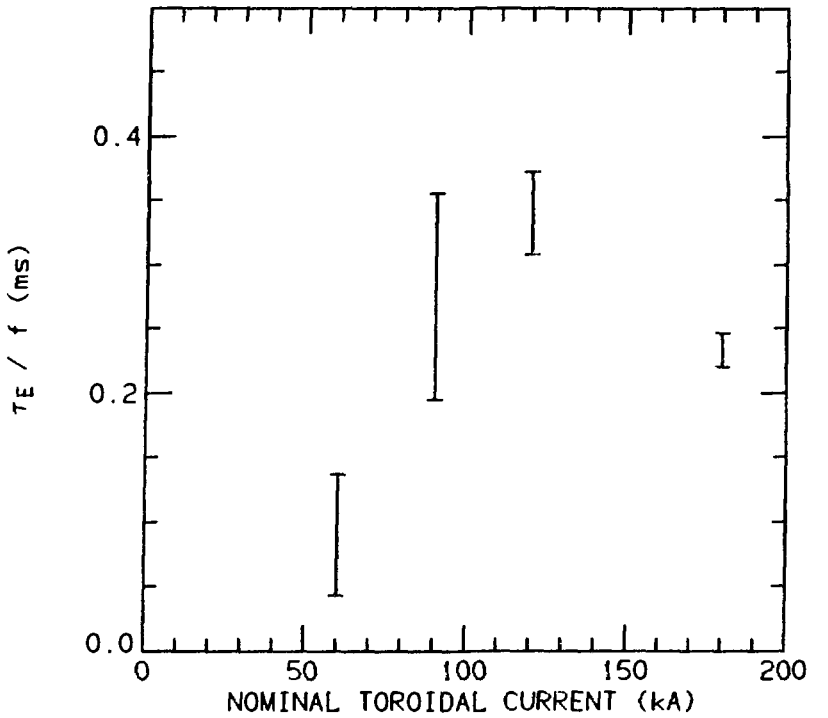

Fig. 34(a). Energy containment time, normalized to the form factor *f*, vs nominal toroidal current. Phase III data at 5 ms.

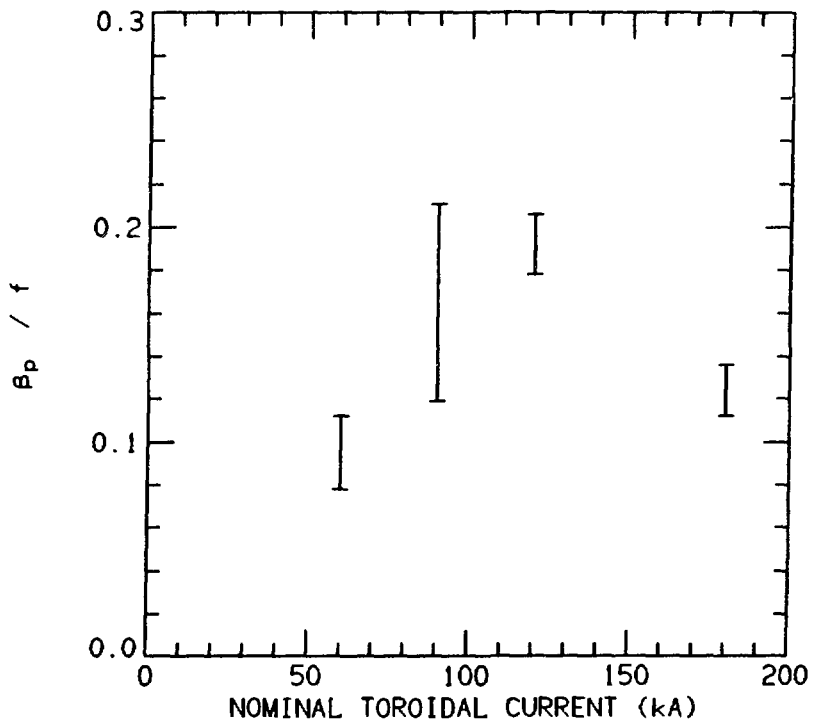

Fig. 34(b). Poloidal beta, normalized to the form factor *f*, vs nominal toroidal current. Same conditions as in Fig. 34(a).

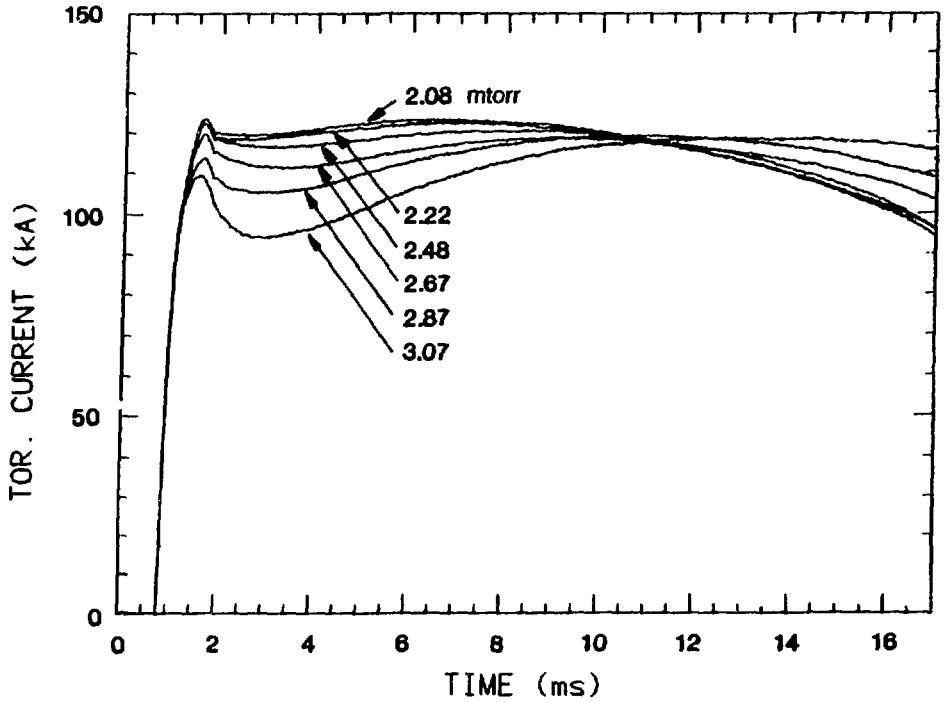

Fig. 35. Toroidal current traces at deuterium fill pressures of 2.08 to 3.07 mtorr. Phase II data.

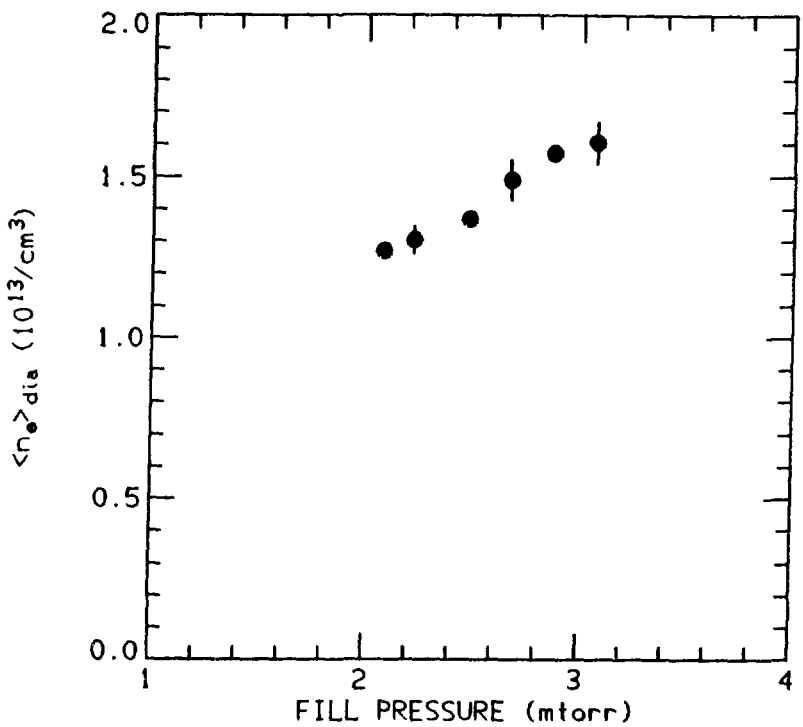

Fig. 36. Diameter-averaged electron density vs fill pressure for the discharge conditions of Fig. 35. Phase II data at 5 ms.

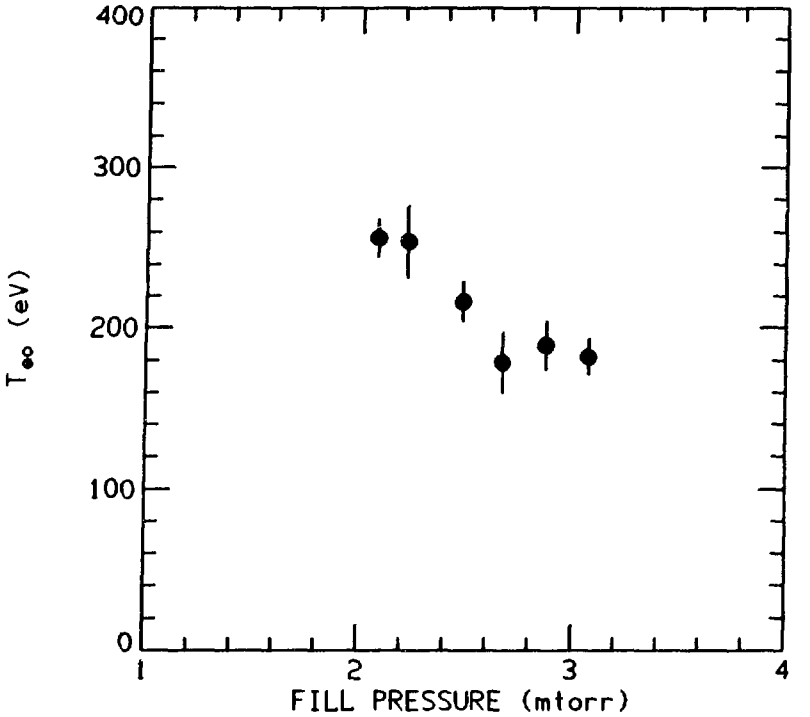

Fig. 37. Central electron temperature vs fill pressure for the discharge conditions of Fig. 35. Phase II data at 5 ms.

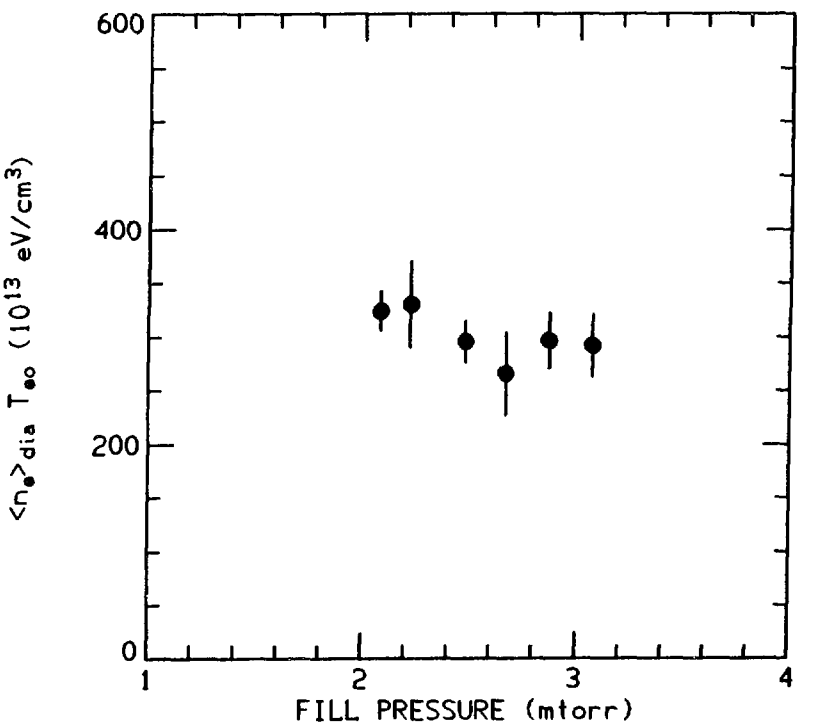

Fig. 38. Product of the diameter-averaged electron density and the central electron temperature vs fill pressure for the discharge conditions of Fig. 35. Phase II data at 5 ms.

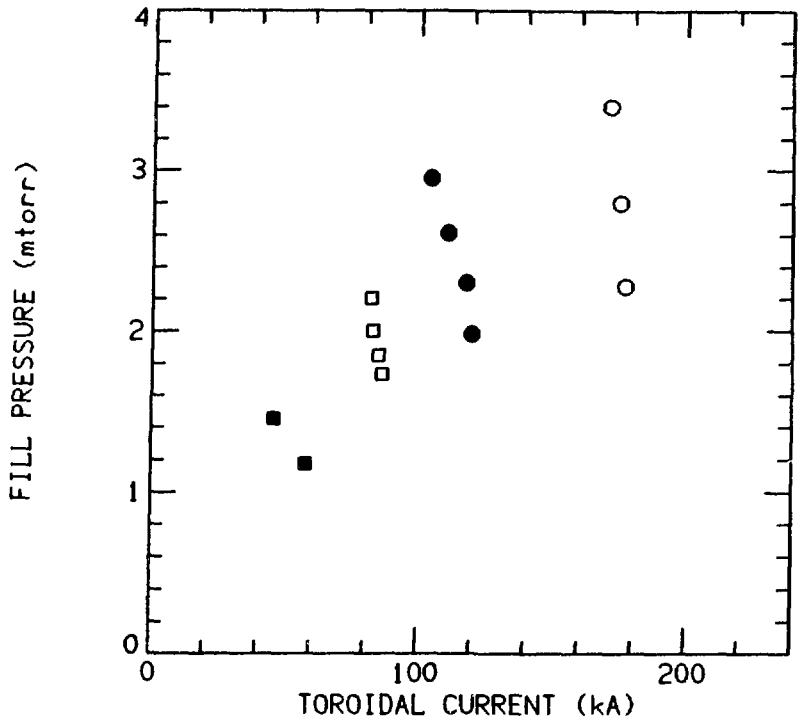

Fig. 39. Deuterium fill pressures, used during Phase III pressure scans, vs toroidal current, at 5 ms. Nominal toroidal currents: 60 kA (solid squares), 90 kA (open squares), 120 kA (solid circles), and 180 kA (open circles).

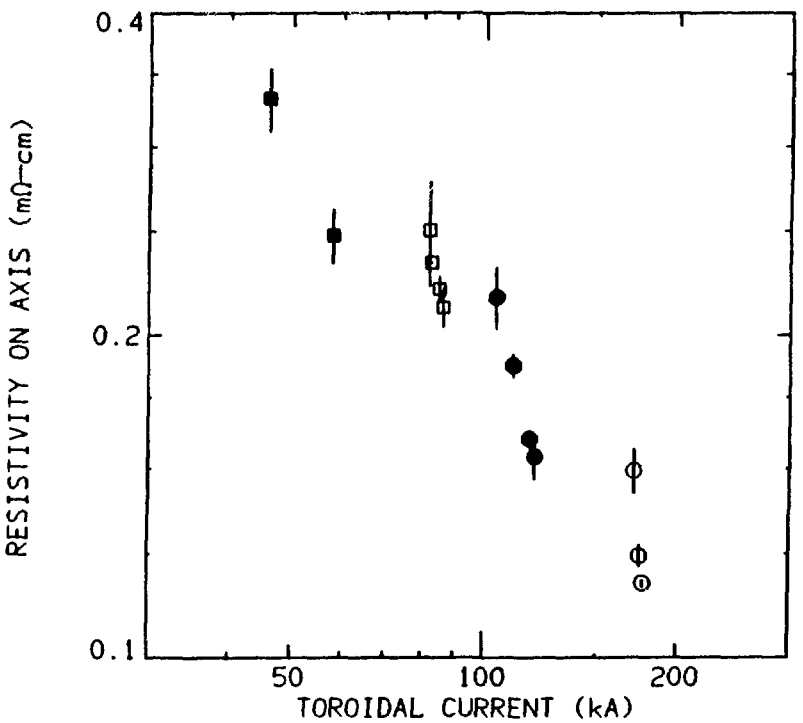

Fig. 40. Effective resistivity on axis obtained under the discharge conditions of Fig. 39. Phase III data at 5 ms.

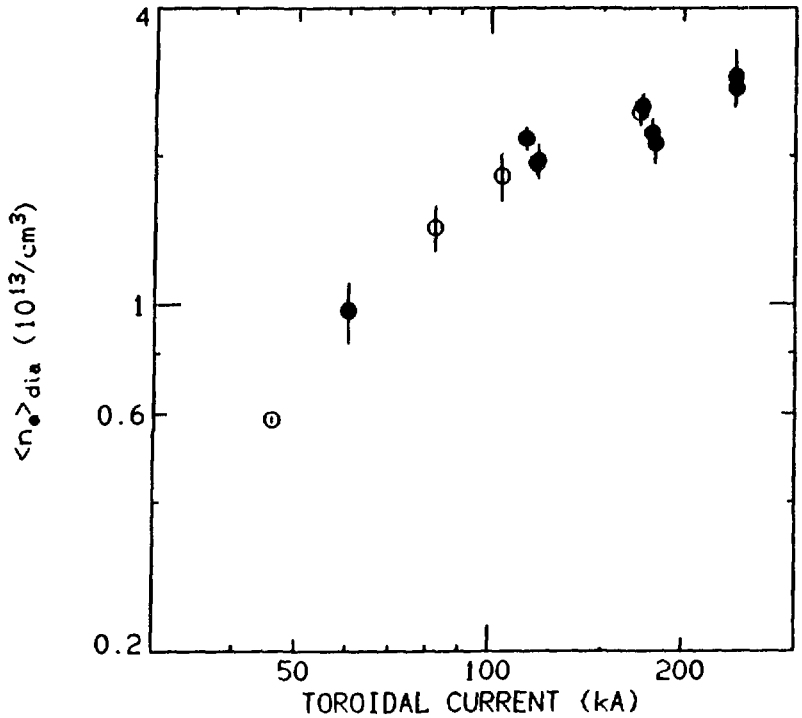

Fig. 41. Diameter-averaged electron density vs toroidal current at high density. Open circles measured at 5 ms at the highest fill pressures of Fig. 39. Solid circles obtained at 3 ms under standard discharge conditions of Phases I and II.

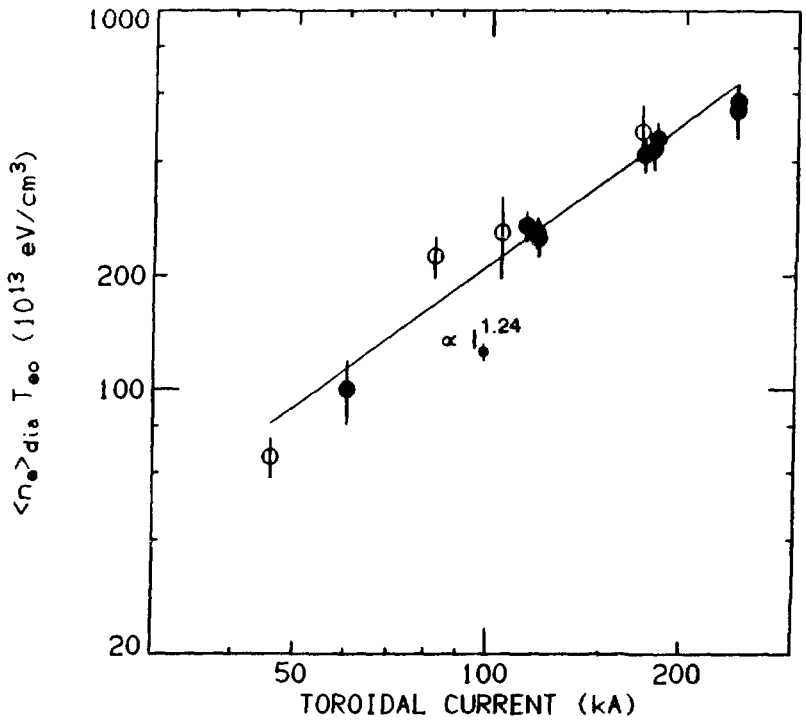

Fig. 42. Product of the diameter-averaged electron density and the central electron temperature vs toroidal current at high density. Same conditions as in Fig. 41.

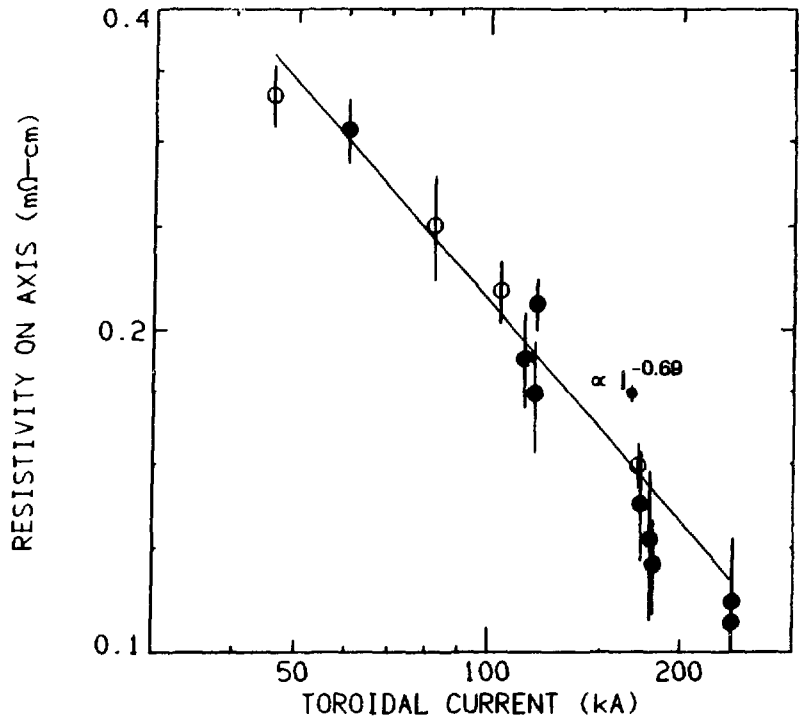

Fig. 43. Effective resistivity on axis vs toroidal current at high density. Same conditions as in Fig. 41.

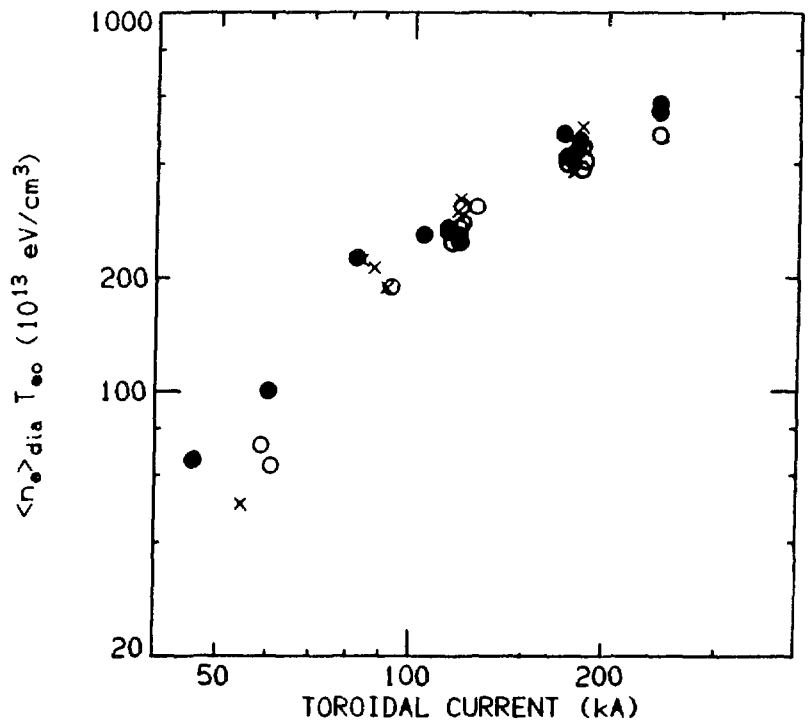

Fig. 44. Product of the diameter-averaged electron density and the central electron temperature vs toroidal current under three discharge conditions. Phases I and II (open circles), Phase III (crosses), and high-density discharges (solid circles).

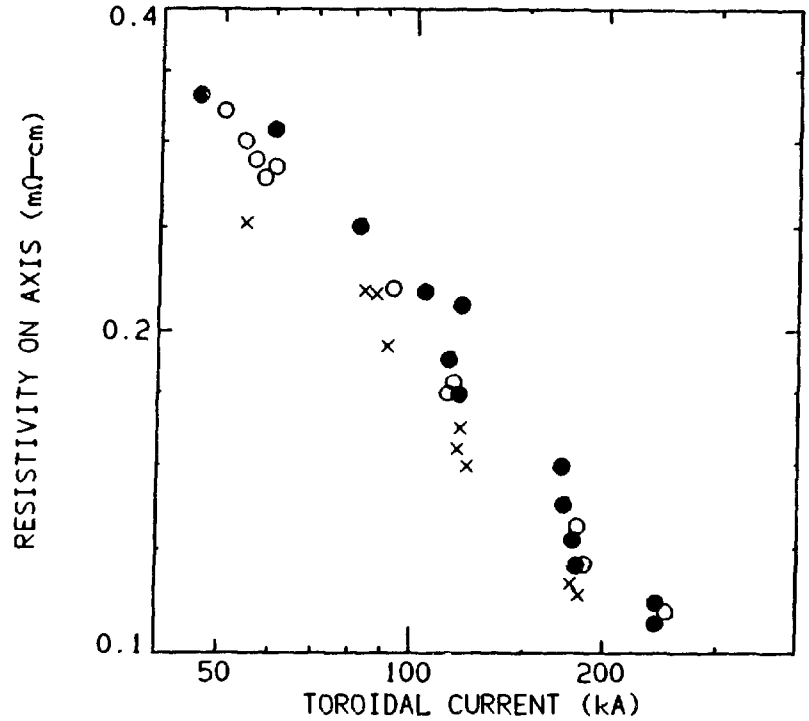

Fig. 45. Effective resistivity on axis vs toroidal current under three discharge conditions. Phases I and II (open circles), Phase III (crosses), high-density discharges (solid circles).

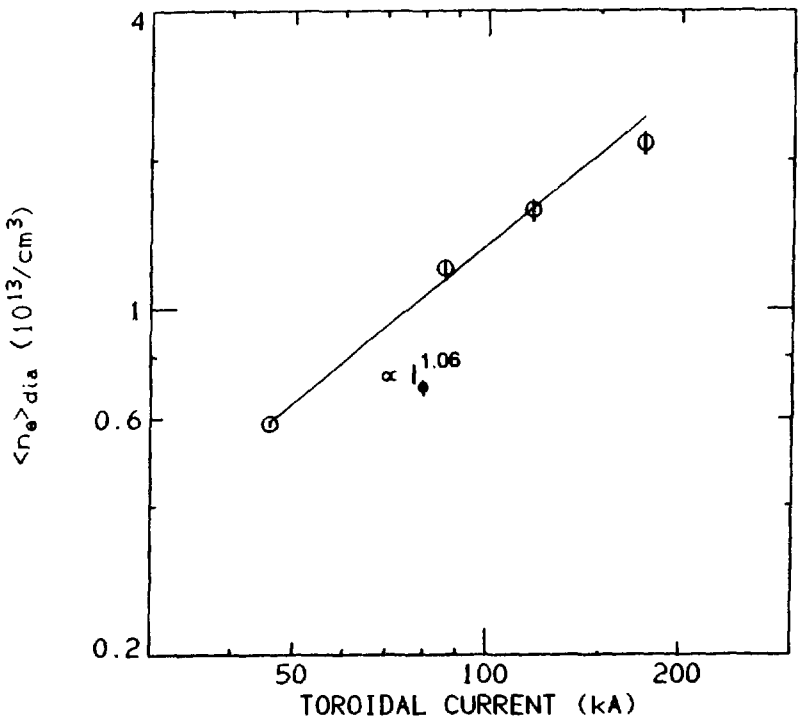

Fig. 46. Diameter-averaged electron density vs toroidal current at approximately constant I_ϕ/N_e. Data taken at 5 ms.

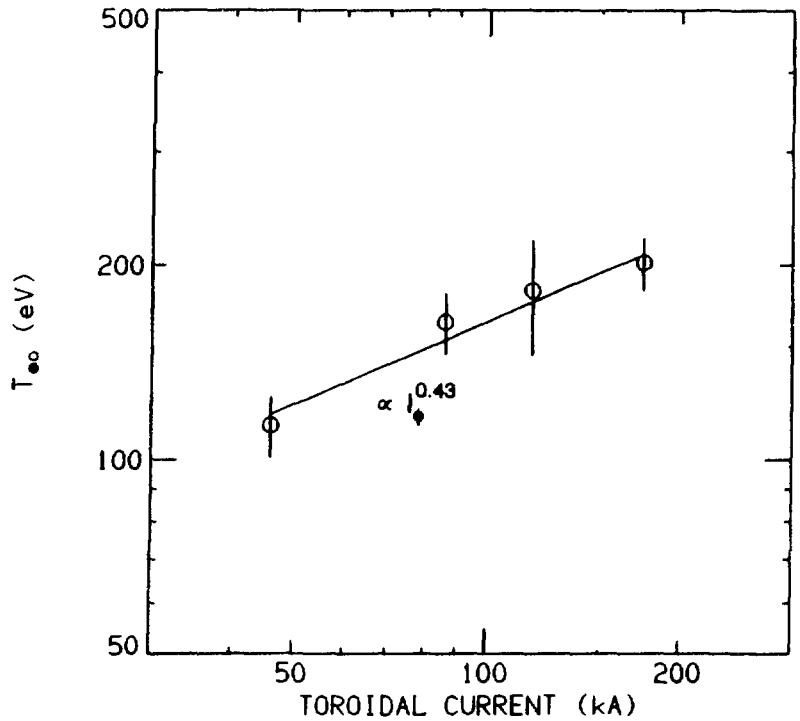

Fig. 47. Central electron temperature vs toroidal current at approximately constant I_ϕ/N_e. Data taken at 5 ms.

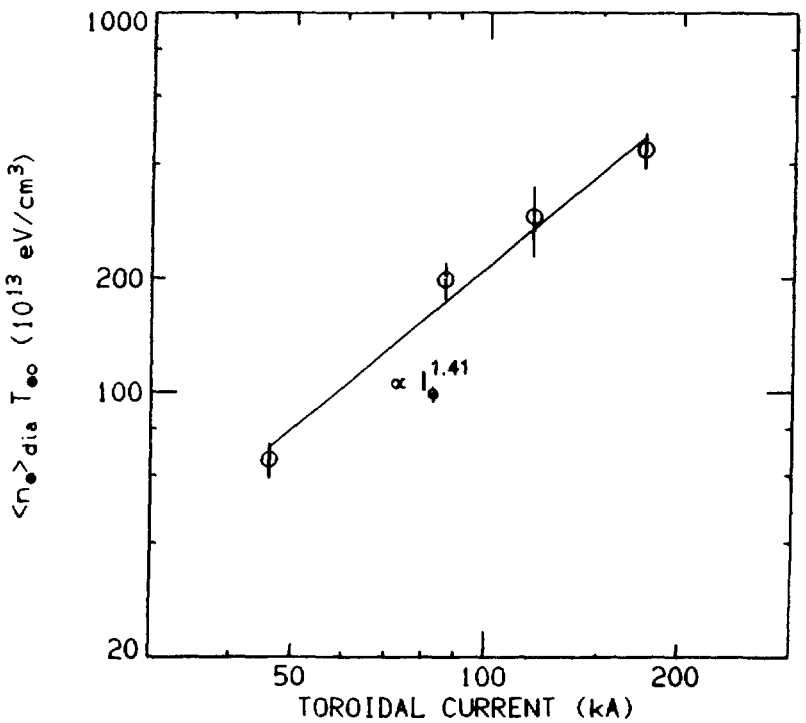

Fig. 48. Product of the diameter-averaged electron density and the central electron temperature vs toroidal current at approximately constant I_ϕ/N_e. Data taken at 5 ms.

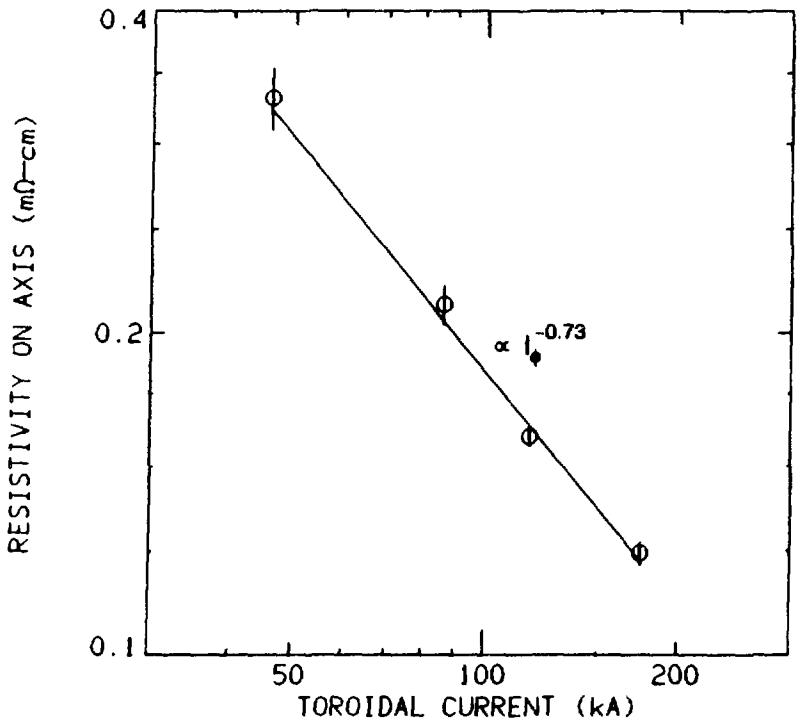

Fig. 49. Effective resistivity on axis vs toroidal current at approximately constant I_ϕ/N_e. Data taken at 5 ms.